Decomplexation as a rate-limitation in the Thiol-Michael addition of N-acrylamides

Joseph S. Brown,[†,‡,a] Andrew W. Ruttinger,[‡,a] Akash J. Vaidya,[a] Christopher A. Alabi[*,a] and Paulette Clancy,[*,b]

‡ Contributed equally to this work
***** Corresponding Authors: caa238@cornell.edu (experimental), pclancy3@jhu.edu (computational)
a Robert F. Smith School of Chemical and Biomolecular Engineering, Cornell University, Ithaca, NY, USA, 14853
b Department of Chemical and Biomolecular Engineering, Johns Hopkins University, Baltimore, MD, USA, 21218
† Present address: Department of Chemistry, Massachusetts Institute of Technology, Cambridge, MA, USA

Supporting Information

Table of Contents

Bimolecular rate equation

The following mass action kinetics were assumed and subsequently solved to determine an analytical solution for nonlinear regression fitting to experimental data.

$$F + M \overset{k_{obs}}{\rightarrow} FM$$

where *F* is the concentration of the fluorous thiol, *M* is the concentration of the *N*-allyl-*N*-acrylamide monomer, and *FM* is the concentration of the product. This results in the following rate equations, leading to a integrated analytical solution of the bimolecular rate equation.

$$\frac{dFM}{dt} = k_{obs}(F)(M)$$

$$F_{total} = F(t=0)\ or\ F_o = F + FM \quad \therefore \quad F = F_o - FM$$

$$M_{total} = M(t=0)\ or\ M_o = M + FM \quad \therefore \quad M = M_o - FM$$

$$\frac{dFM}{dt} = k_{obs}\left(F_{total} - FM\right)\left(M_{total} - FM\right)$$

$$\int \frac{dFM}{\left(F_{total} - FM\right)\left(M_{total} - FM\right)} = \int kdt$$

$$\frac{FM - F_o}{FM - M_o} = C \cdot exp\left(kt\left(F_o - M_o\right)\right),\ where\ C\ is\ a\ constant\ from\ integration$$

$$FM(t=0) = 0 \quad \therefore \quad C = \frac{F_o}{M_o}$$

$$\frac{FM - F_o}{FM - M_o} = \frac{F_o}{M_o} exp\left(kt\left(F_o - M_o\right)\right)$$

$$FM = \frac{F_o M_o[\exp\left(kt\left(F_o - M_o\right)\right) - 1]}{F_o \exp\left(kt\left(F_o - M_o\right)\right) - M_o}$$

All kinetic data gathered were normalized between 0 and 1, where 0 represents the start of the reaction (no conversion), and 1 represents the complete conversion to the product of the resulting fluorous tagged olefin. Thus, this equation was normalized to the reaction by F_o.

$$\frac{FM}{F_o} = \frac{M_o[\exp\left(kt\left(F_o - M_o\right)\right) - 1]}{F_o \exp\left(kt\left(F_o - M_o\right)\right) - M_o}$$

Quantification of thiol concentration by 2,2' dithiodipyridine (DTDP)

Thiol concentration was quantitatively assessed during the thiol-Michael addition by modification from previous reported literature.[1,2] Assay concentration was designed to be 100uM final, with a final volume of 210uL. Microcentrifuge tubes held the bulk of the assay volume of 1.4 mL, constituted from 45 µL 12mM 2,2' dithiodipyridine (386 µM final) and 1350.1 µL 0.1 v/v% triethylamine (TEA) in DMSO. Time-point aliquots (4.9 µL) were taken from the reaction containing the prospective fluorous thiol at a reaction concentration of 30mM. The initial (t=0) time-point was taken before the reaction was started (43.9 mM) and diluted appropriately. Preliminary studies showed thiolate concentration was detected by DTDP consistently after being aliquoted into the microcentrifuge tube termed the "thiol incubation." However, there was a modest decrease in detected thiolate concentration after being placed into the 96-well plate with the subsequent acetic acid addition termed the "acid incubation" (Figure S1).

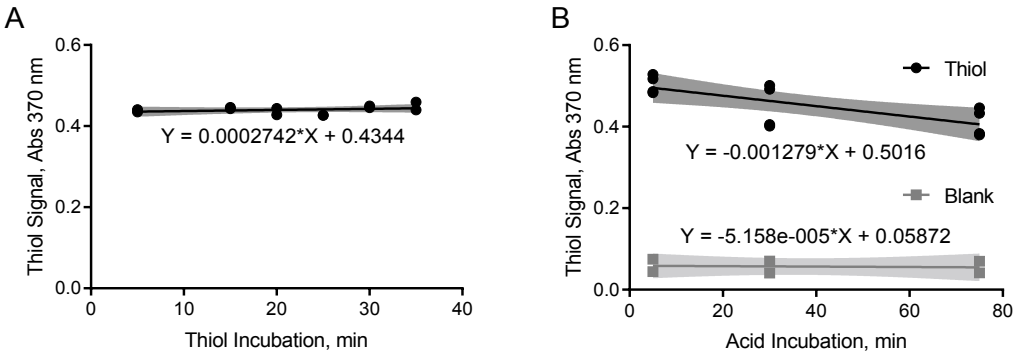

Figure S1. Thiol and acid incubations that affect the DTDP signal **A.** Thiol signal from DTDP absorbance versus thiol incubation time revealing that the fluorous thiol can remain in the DTDP assay for long periods of time without affecting the resulting signal (F test for significantly non-zero slope, $p = 0.3652$, $n = 2$, $df = 1$). **B.** Thiol signal from DTDP absorbance versus acid incubation time revealing the fluorous thiol signal decreases modestly over time in the presence of acid (F test for significantly non-zero slope, $p = 0.0076$, $n = 2$, $df = 1$) while the blank remains constant (F test for significantly non-zero slope, $p = 0.8492$, $n = 2$, $df = 1$). The shaded area is the 95% CI around the linear regression line.

Thus, from the 1.4mL bulk assay volume, 200 µL was transferred to a Grenier or Corning 96-well UV-transparent flat plate or a ThermoFisher Scientific flat 96-well plate and 10 µL of acetic acid was added immediately before reading sample absorbance (370±5 nm) using a multi-channel pipette. Samples were normalized to 450 nm to account for well-to-well variation in the 96-well plate, where no absorbance of the reaction substituents was observed, and blank subtracted. Plate reader measurements were completed utilizing a TECAN Infinite M1000 PRO Microplate Reader (Männdorf, Switzerland). Nonlinear regression fitting analysis was performed within GraphPad 7.05 using the F_o-normalized integrated equation described in the methods above to find an apparent rate k_{obs}, reported with standard error.

Verification of Functional Performance for DFT Calculations

Prior to performing any theoretical calculations for comparison with experiment, we sought to verify the performance of our selected density functional approximation. Although range-separated functional are suggested as the best performers for thiol-Michael addition reactions, their computational cost is exceedingly prohibitive as system size increases.[3] In the case of our study, reaching up to 145 atoms, these functionals become impractical. GGA functional provide a fast alternative to these range-separated functionals. In particular, Goerigk et al. show B97-D3 to be one of the most accurate functionals of the GGA class, outperforming more advanced functionals.[4] Maridirossian and Head-Gordon corroborate this, stating that, for GGA functionals, "B97-D3 performs best for thermochemistry and barrier heights" and is "recommended as [one of] the default choices from this class." [5] However, GGA functionals have also been shown to suffer from delocalization error in thiol-Michael addition systems.[3,6] Then, benchmarking the performance of these GGA functionals in our system is both prudent and necessary.

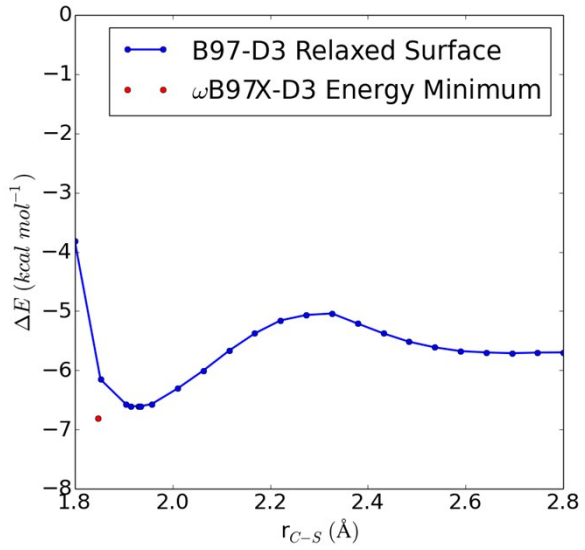

Figure S2. Our relaxed surface scan of the C-S bond between methyl thiolate and methyl vinyl ketone using the B97-D3 functional with the def2-TZVP basis set and CPCM implicit methanol solvent. The carbanion structure was also optimized using the ωB97X-D3 functional for direct comparison between predicted binding energies of the functionals.

All our preliminary verification calculations were performed using the Orca software package[7]. In addition to the B97-D3 functional,[8] we also employed Ahlrichs' def2-TZVP basis set[9–11] using the CPCM implicit solvation model for approximation of a methanol solvent.[12] To expressly validate these selections, we performed a relaxed surface scan to determine the C-S bond length and corresponding reaction energy between methyl thiolate and methyl vinyl ketone based on the study by Smith *et al.* for evaluating functionals in thiolate systems.[3] Importantly, our results show a clear, carbanion intermediate. Moreover, our predicted C-S bond length is 1.93 Å (Figure S2), in excellent agreement with Smith *et al.*'s prediction of 1.92 Å.[3] Our use of an implicit methanol solvent did not allow for direct comparison of energies between our results and Smith

et al. To rectify this, we also calculated the energy minimum for the ωB97X-D3 functional in the implicit methanol solvent. Our results show excellent agreement, predicting a binding energy of -6.6 kcal/mol for the B97-D3 functional versus -6.8 kcal/mol for the ωB97X-D3 functional. The C-S bond length predicted by the ωB97X-D3 functional contracts slightly to 1.84 Å, still in good agreement with the 1.93 Å bond length predicted by the B97-D3 functional. Based on these results, we are confident that our choice of functional reflects the proper behavior in our thiol-Michael addition system.

NEB simulation

All NEB simulations for our study were performed using our custom NEB algorithm for compatibility with the Orca DFT software package.[7] These calculations were performed at the B97-D3 level of theory[8] with Ahlrichs' def2-TZVP basis set.[9–11] We chose the LBFGS optimizer[13] based on the recommendation from Herbol *et al.*[14] A spring constant, required for the harmonic spring force, was chosen to be 0.1 eV/Å. We used the Climbing-Image NEB algorithm,[15] which came into effect after five iterations of the NEB optimizer, to provide an accurate guess of the transition state atomic geometry. Additional parameters included a dimensionless step size, dimensionless step size adjustment, and maximum step size of 1.0, 0.5, and 0.04 Å, with an accelerated line-search method for faster convergence. The step size was reset every 20 steps. For all energy barriers, the convergence criterion was either a root mean squared force of 0.0272 Ha/Å or a maximum force of 0.0272 Ha/Å. In cases where the potential energy surface was fairly flat, the convergence criterion was loosened slightly due to convergence issues. An example of the NEB method for the propagation step in the butyl *N*-allyl-*N*-acrylamide monomer reaction is shown in Figure S2. The transition state corresponds to an x-value of 6 along the reaction coordinate.

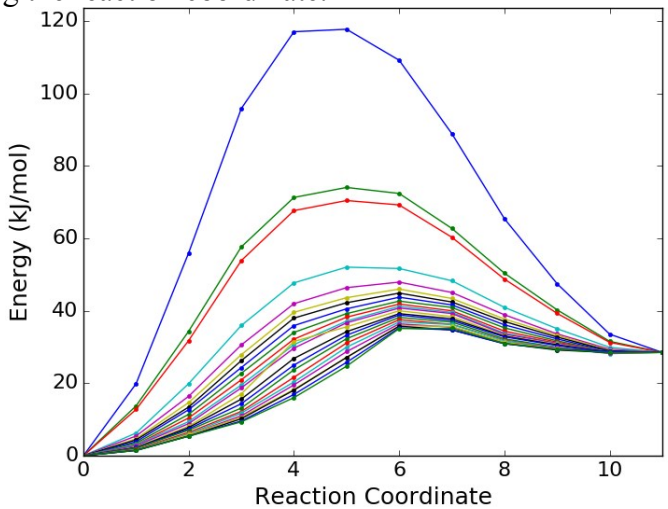

Figure S3. Iterative reduction of energy using our custom NEB method. The figure shows the propagation step of the butyl *N*-allyl-*N*-acrylamide, calculated using the B97-D3 functional with the def2-TZVP basis set and an implicit methanol solvent. Colors show the energy barrier at each iteration, moving downward to the final energy barrier of 38 kJ/mol.

Alternative pathway for thiol-Michael addition

A recent study highlighted a potential alternate mechanism for the reaction between a thiolate and phosphonium ester salt.[16] Rather than undergoing the traditional thiol-Michael

addition reaction, the phosphonium ester salt would undergo a substitution between the dimethylphenylphosphine and the thiolate. To ensure that the reaction mechanism we studied is the MEP, we evaluated the energy barrier of this substitution reaction. Using NEB, we found that the energy barrier is high (217 kJ/mol), much larger than our experimentally observed energy barriers. This is likely due to the high energy configuration of the complex formed between the allylacrylamide, DMPP, and thiolate during reaction.

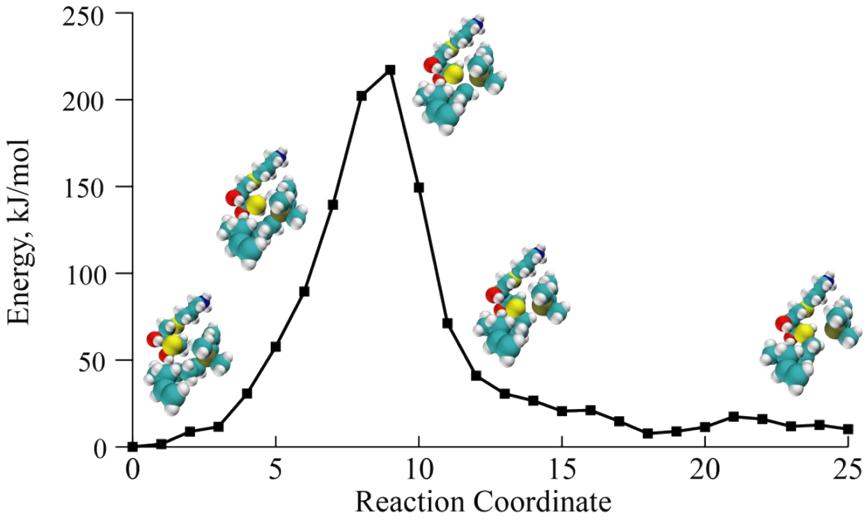

Figure S4. Energy barrier for the substitution reaction between the allylacrylamide, DMPP, and thiolate. Snapshots of the reactive complex are shown along the reaction coordinate.

Analysis of aromatic stacking

To compare stacking configurations for the benzyl *N*-allyl-*N*-acrylamide and the ethylenephenyl *N*-allyl-*N*-acrylamide, we evaluated the angle between the stacking benzene rings and the distances between their center of masses. Angles close to 90˚ denote a T-stacking configuration while angles close to 0˚ denote a parallel-displaced configuration. Center of mass distances were calculated for comparison with literature.[17]

Table S1. Angle between stacking benzene rings for each stable complex along the reaction coordinate of the thiol-Michael addition for the benzyl *N*-allyl-*N*-acrylamide and the ethylenephenyl *N*-allyl-*N*-acrylamide.

State Along Reaction Coordinate	Benzyl	Ethylenephenyl
Reactant	12.1˚	88.4˚
Intermediate after Initiation	9.1˚	85.2˚
Intermediate after Propagation	46.9˚	45.5˚
Intermediate after Chain Transfer	26.3˚	N/A

Table S2. Center of mass distances between stacking benzene rings for each stable complex along the reaction coordinate of the thiol-Michael addition for the benzyl *N*-allyl-*N*-acrylamide and the ethylenephenyl *N*-allyl-*N*-acrylamide. For the benzyl *N*-allyl-*N*-acrylamide, which exists

in a parallel-displaced configuration, the parallel offset distance between the center of masses of the benzene rings is shown in brackets.

State Along Reaction Coordinate	Benzyl	Ethylenephenyl
Literature[17]	3.76 Å (3.4 Å)	4.9 Å
Reactant	4.00 Å (3.67 Å)	5.03 Å
Intermediate after Initiation	4.03 Å (3.63 Å)	5.00 Å
Intermediate after Propagation	5.43 Å (2.69 Å)	4.82 Å
Intermediate after Chain Transfer	5.05 Å (3.67 Å)	6.22 Å

Kinetic evaluation of dimethyl phenyl phosphine and *N*-allyl-*N*-acrylamides.

The reaction to form the initiator was investigated. In particular, we sought to examine the kinetics of the reaction to verify that the initiator was completely formed within the 15-minute incubation period.

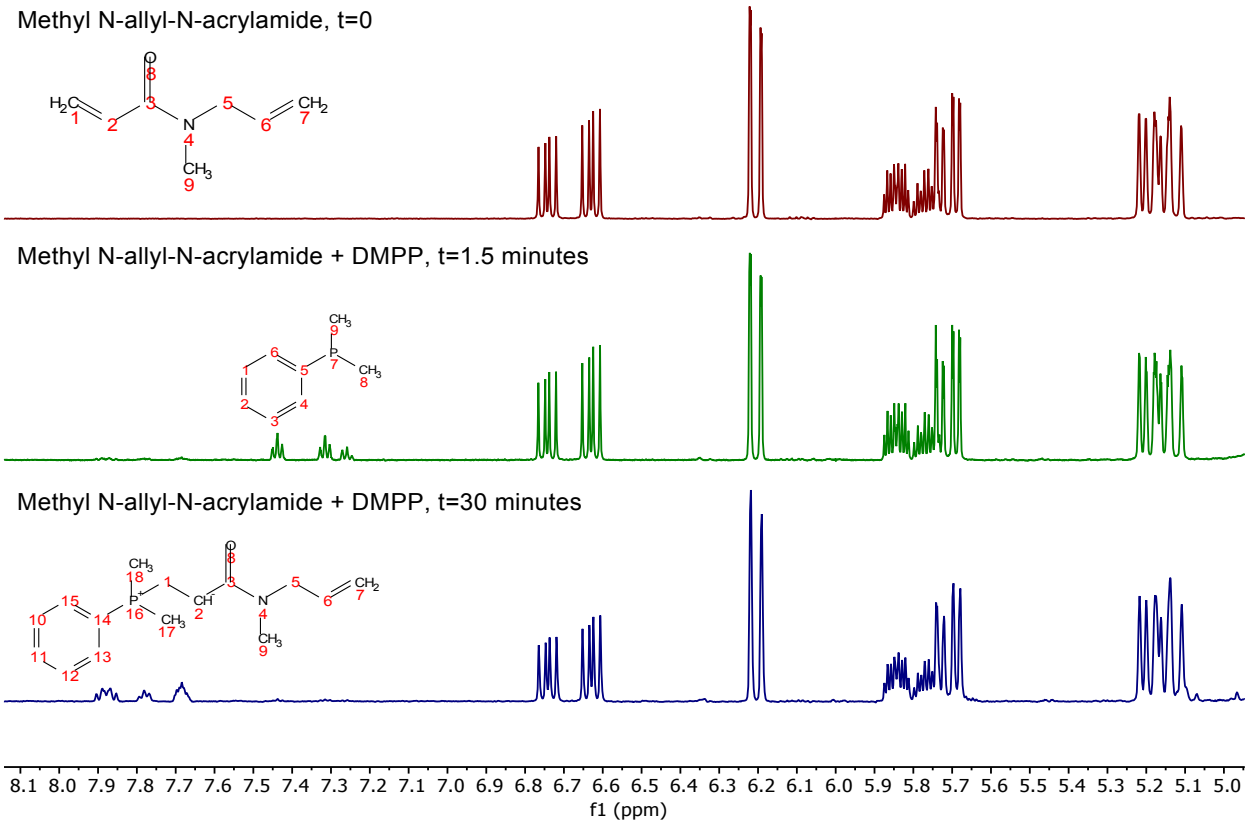

Figure S5. Selected ^{1}H NMR (600 MHz) in 10% CH_3OH in CD_3OD at ZOOMED x- and y-scale of the reaction between the dimethylphenyl phosphine and the methyl *N*-allyl-*N*-acrylamide. Spectra shown are of the methyl *N*-allyl-*N*-acrylamide starting material (top), 1.5 minutes after the addition of dimethylphenyl phosphine (DMPP) with the DMPP aromatic peaks appearing around 7.35ppm, and after 30 minutes of reaction showing the reaction appears practically complete.

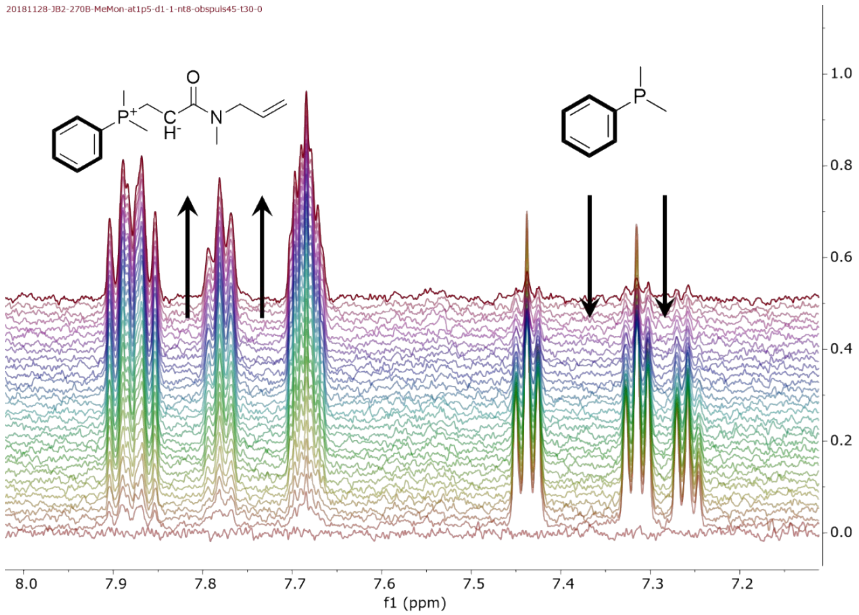

Figure S6. Reaction of dimethylphenyl phosphine (DMPP) with the Methyl-*N*-allyl-*N*-acrylamide to prepare the initiator by ^{1}H NMR. A low monomer concentration was used (20 mM) to enable accurate observation of this quick reaction with 5 mol% DMPP in 10% MeOH in d-MeOD at room temperature. Some decrease in reaction rate could be expected with the addition of deuterium in place of the proton onto the acrylamide after the attack of the phosphine; therefore, this kinetic rate represent a conservative estimate.

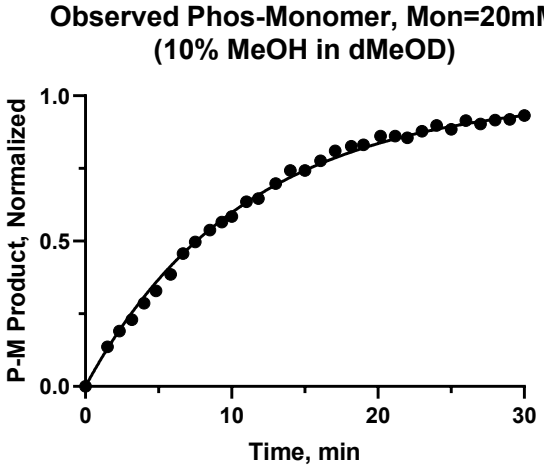

Figure S7. Integrated areas of the product of dimethylphenyl phosphine and the Methyl-*N*-allyl-*N*-acrylamide with a bimolecular fit showing excellent agreement. Each data point represents the integration area from 7.65 to 7.95 ppm, with normalization provided from the consumption of the starting material DMPP in 7.2 to 7.5 ppm. (*n=1*, observing 6 distinct peaks as in Figure S10)

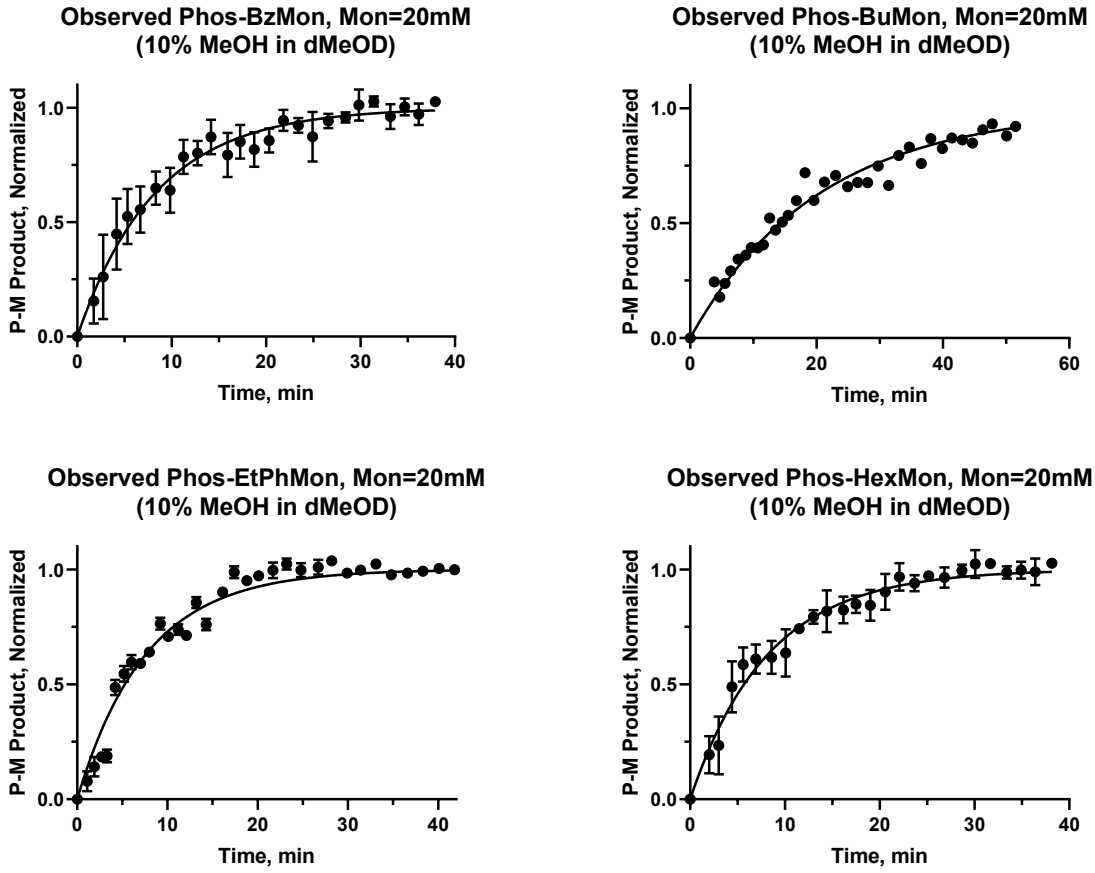

Figure S8. ^{1}H NMR kinetic experiments of other *N*-allyl-*N*-acrylamides utilized in this study reacting at 20 mM) with 5 mol% DMPP in 10% MeOH in d-MeOD at room temperature. Each data point represents the integration area from 7.65 to 7.95 ppm, with normalization provided from the consumption of the starting material DMPP in 7.2 to 7.5 ppm, separate from monomer peaks in the case of the aromatic monomers. Error bars represent the experimental error of measurement (*n=1* for all. Benzyl: 3 product peaks were distinctly observed apart from other aromatic peaks from the monomer. Butyl: 3 product peaks distinctly observed as in Figure S10. Ehtylenephenyl: 2 product peaks were distinctly observed. Hexyl: 3 product peaks distinctly observed as in Figure S10.)

Summary of kinetic results.

Table S3. Summary of kinetic study of *N*-allyl-*N*-acrylamide reaction with DMPP, summarizing Figure S10 through Figure S12.

Kinetic Rate of Reaction of Monomer with DMPP (M^{-1} s^{-1}).

	Methyl	Benzyl	EthPhenyl	Butyl	Hexyl
k, M^{-1} s^{-1}	0.0773	0.0981	0.111	0.0412	0.103
SE	0.0007	0.0041	0.0036	0.0010	0.0030

Time to 99% conversion in DTDP assay conditions (120mM) from bimolecular equation.

	Methyl	Benzyl	EthPhenyl	Butyl	Hexyl
Time, min	8	6.5	5.5	15	6

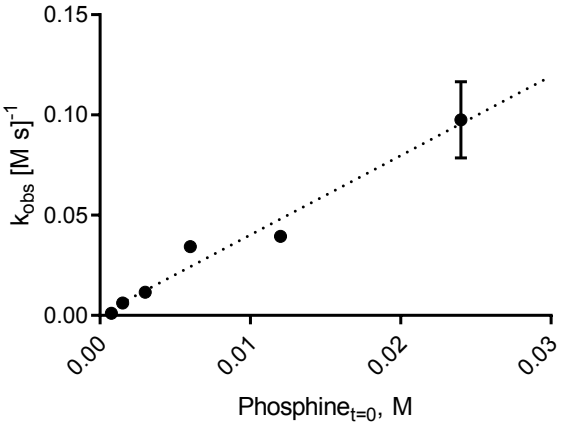

Figure S9. Observed reaction rate versus DMPP concentration for the thiol-Michael addition of the methyl *N*-allyl-*N*-acrylamide and fluorous DTT.

Summary of kinetic reaction rate data.

Table S4. Summary of kinetic reaction rate data from Figure 2.

DTDP, Bimolecular k_{app}

	RT (25ºC)			40ºC		
Monomer	k, 1/M*s	SE	Independent replicates (*n*)	k, 1/M*s	SE	Independent Replicates (*n*)
MeMon	1.15E-02	4.92E-04	6	3.10E-02	1.01E-03	4
BuMon	3.09E-03	2.24E-04	3	1.10E-02	9.33E-04	3
HexMon	4.37E-03	4.82E-04	3	1.50E-02	1.73E-03	3
PhEtMon	1.35E-02	1.28E-03	3	2.76E-02	1.42E-03	2
BzMon	3.26E-03	2.48E-04	2	4.37E-02	5.54E-03	3
FBT-MeMon	9.01E-04	6.96E-05	2	1.45E-03	7.42E-05	2

Table S5. Statistical analysis of kinetic reaction rate data from Figure 2

Species		Temp, C	Significance	P-value	Type (of T-test)	df
Methyl	Butyl	25	***	0.0002	Two-tailed, Welch's correction	2.795
		40	****	<0.0001	Two-tailed, Welch's correction	3.975
	Hexyl	25	****	<0.0001	Two-tailed, Welch's correction	3.998
		40	***	0.0006	Two-tailed, Welch's correction	3.221
	EtPhenyl	25	ns	0.1046	Two-tailed, Welch's correction	2.612
		40	ns	0.2040	Two-tailed, Welch's correction	2.516
	Beznyl	25	***	0.0001	Two-tailed, Welch's correction	2.955
		40	ns	0.0538	Two-tailed, Welch's correction	2.133
Butyl	Hexyl	25	*	0.0282	Two-tailed, Welch's correction	2.825
		40	*	0.0373	Two-tailed, Welch's correction	3.073
Benzyl	EtPhenyl	25	**	0.0036	Two-tailed, Welch's correction	2.218
		40	*	0.0260	Two-tailed, Welch's correction	2.565

Significance scale: ns = not significant, P-value ≥ 0.05; * = significant, P-value ranges 0.05 – 0.01; ** = very significant, P-value ranges 0.01 – 0.001; *** and **** = extremely significant, P-value ranges 0.001 – 0.0001, with **** representing P-values ≤ 0.0001.

Calculation of activation energies from kinetic data

These kinetic data at two temperatures were used with the Eyring equation with the substitution of the Gibb's free energy equation to calculate the activation energy (enthalpy). The Eyring equation was preferred over the Arrhenius equation, as it provides the free energy of reaction and is derived empirically, whereas the Eyring equation is only based on the assumptions of transition state theory. Specifically:

$$k_x = \frac{\kappa k_B T_x}{h} exp(\frac{-\Delta G^{\ddagger}}{RT_x})$$

$$\ln\left(\frac{k_x}{T_x}\right) = \ln\left(\frac{\kappa k_B}{h}\right) + \frac{\Delta S}{R} + \frac{\Delta H^{\ddagger}}{RT_x}$$

$$\Delta H^{\ddagger} = \frac{-R[\ln\left({}^{k_1}/_{T_1}\right) - \ln\left({}^{k_2}/_{T_2}\right)]}{({}^{1}/_{T_1} - {}^{1}/_{T_2})}$$

Where k_x is the kinetic rate (x = kinetic point 1 or 2 for temperature 1 and 2), κ is the transmission coefficient, k_B is Boltzmann's constant, h is Planck's constant, T_x is the temperature (either T1 = 22 ºC or T2 = 40 ºC), $\Delta G^{\ddagger}$ is the free energy of the reaction, R is the gas constant, ΔS is the entropy of the reaction, and $\Delta H^{\ddagger}$ is the enthalpy of the reaction.

Raw Observed Kinetic Data.

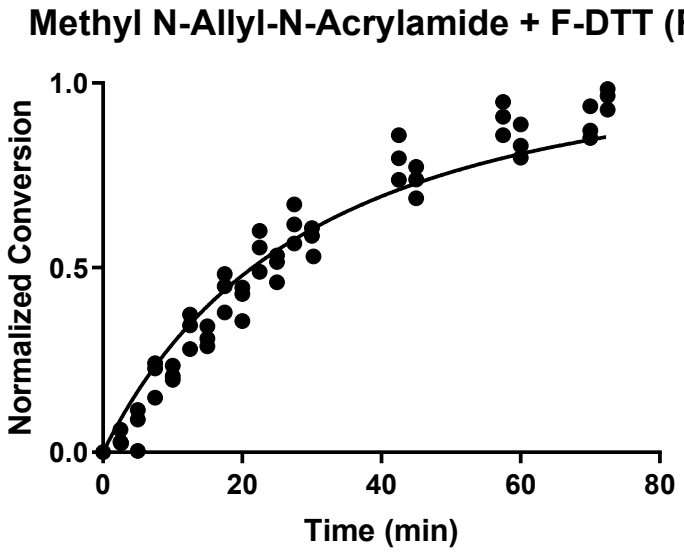

Figure S10. Observed 25°C kinetics by DTDP assay of 30 mM hydroxylated fluorous thiol (F-DTT) with 2 eqv of methyl N-allyl-N-acrylamide catalyzed as described in the Methods (*n=6*).

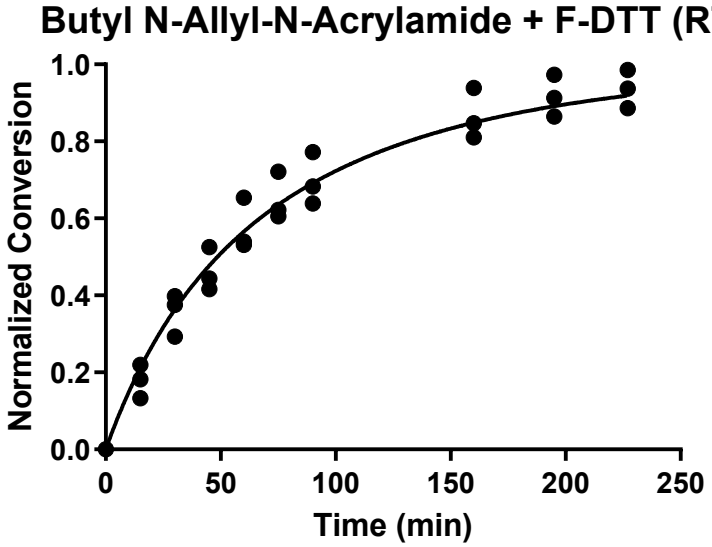

Figure S11. Observed 25°C kinetics by DTDP assay of 30 mM hydroxylated fluorous thiol (F-DTT) with 2 eqv of butyl N-allyl-N-acrylamide catalyzed as described in the Methods (*n=3*).

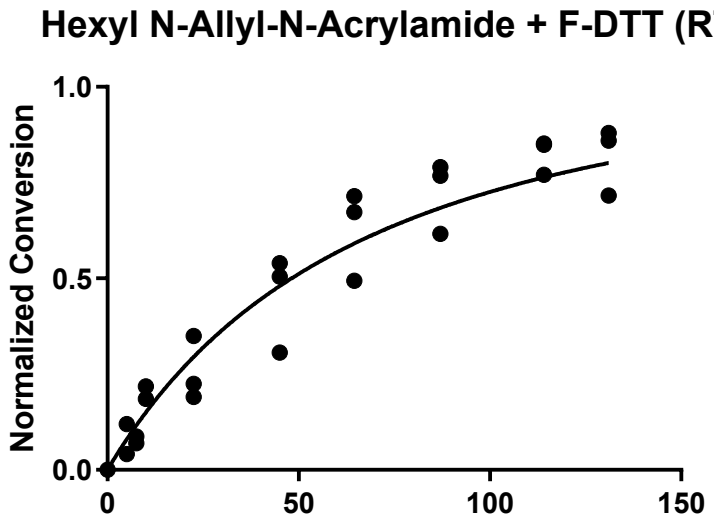

Figure S12. Observed 25°C kinetics by DTDP assay of 30 mM hydroxylated fluorous thiol (F-DTT) with 2 eqv of hexyl N-allyl-N-acrylamide catalyzed as described in the Methods (*n=3*).

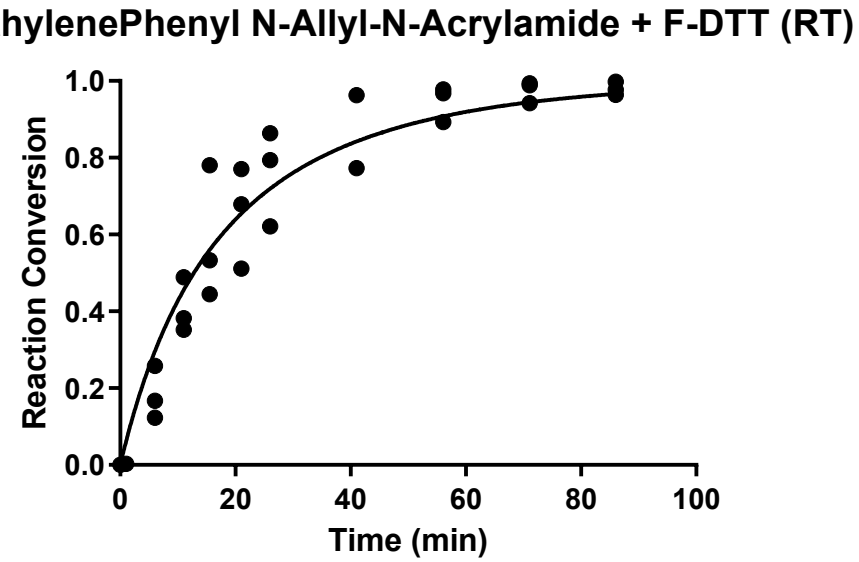

Figure S13. Observed 25°C kinetics by DTDP assay of 30 mM hydroxylated fluorous thiol (F-DTT) with 2 eqv of ethylenephenyl N-allyl-N-acrylamide catalyzed as described in the Methods (*n=3*).

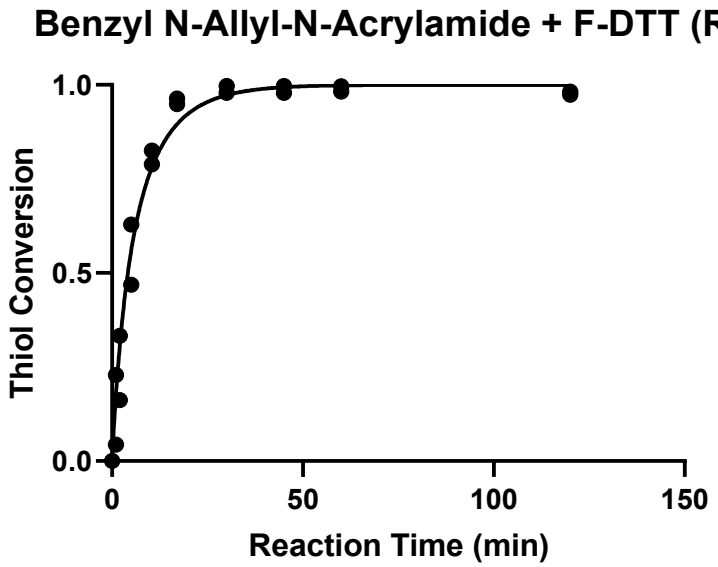

Figure S14. Observed 25°C kinetics by DTDP assay of 30 mM hydroxylated fluorous thiol (F-DTT) with 2 eqv of benzyl N-allyl-N-acrylamide catalyzed as described in the Methods (*n=2*).

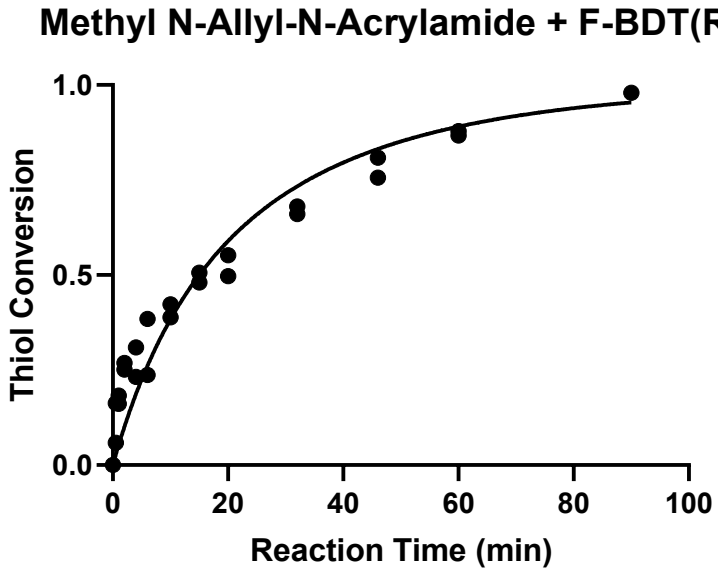

Figure S15. Observed 25°C kinetics by DTDP assay of 30 mM alkyl fluorous thiol (F-BDT) with 2 eqv of methyl N-allyl-N-acrylamide catalyzed as described in the Methods (*n=2*).

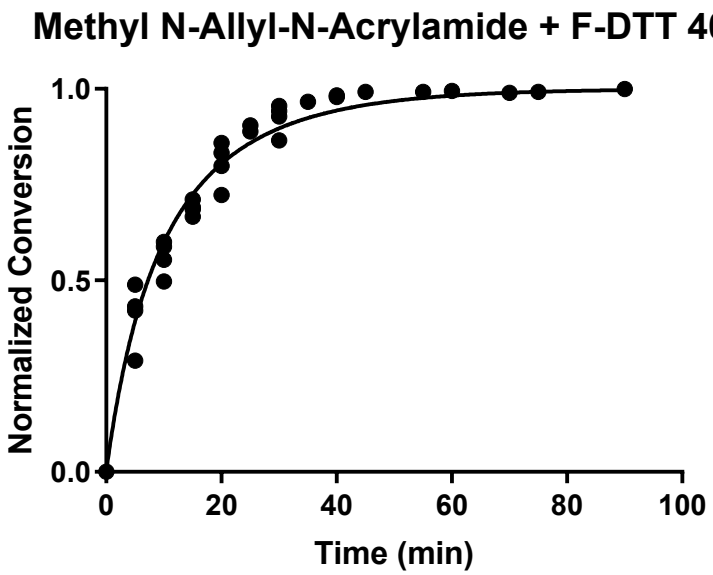

Figure S16. Observed 40°C kinetics by DTDP assay of 30 mM hydroxylated fluorous thiol (F-DTT) with 2 eqv of methyl N-allyl-N-acrylamide catalyzed as described in the Methods (*n=4*).

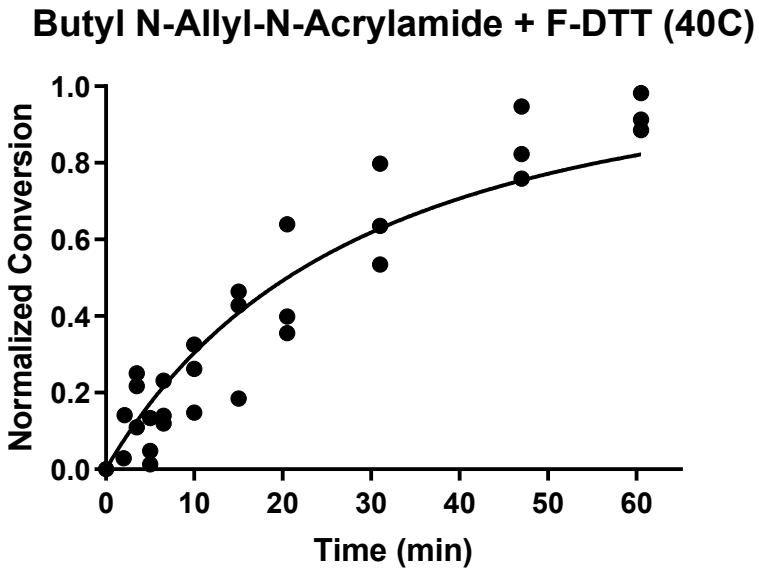

Figure S17. Observed 40°C kinetics by DTDP assay of 30 mM hydroxylated fluorous thiol (F-DTT) with 2 eqv of butyl N-allyl-N-acrylamide catalyzed as described in the Methods (*n=3*).

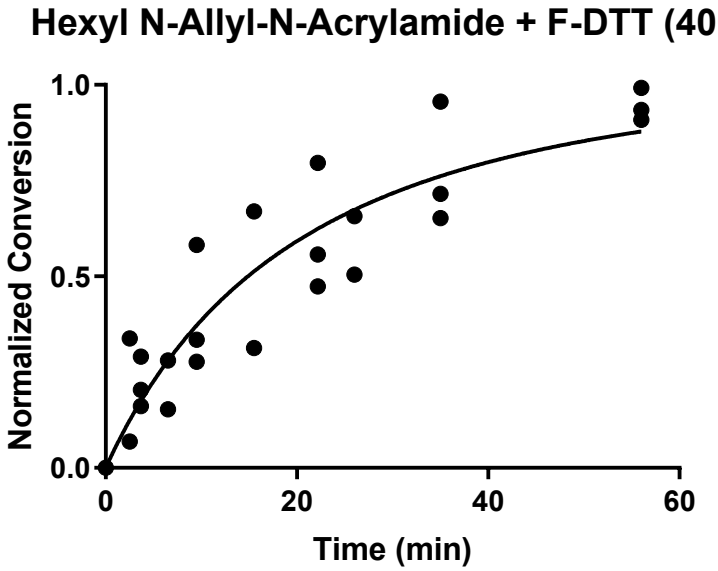

Figure S18. Observed 40°C kinetics by DTDP assay of 30 mM hydroxylated fluorous thiol (F-DTT) with 2 eqv of hexyl N-allyl-N-acrylamide catalyzed as described in the Methods (*n=3*).

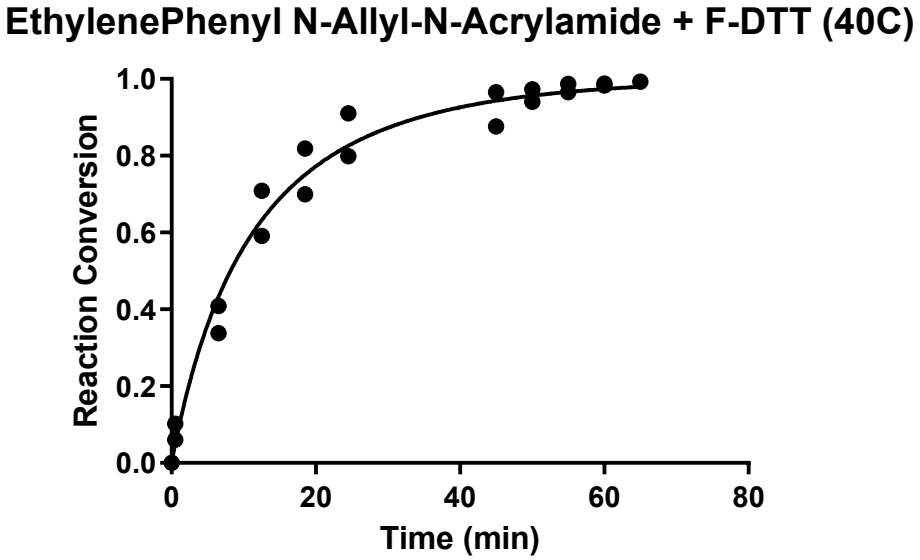

Figure S19. Observed 40°C kinetics by DTDP assay of 30 mM hydroxylated fluorous thiol (F-DTT) with 2 eqv of ethylenephenyl N-allyl-N-acrylamide catalyzed as described in the Methods (*n=2*).

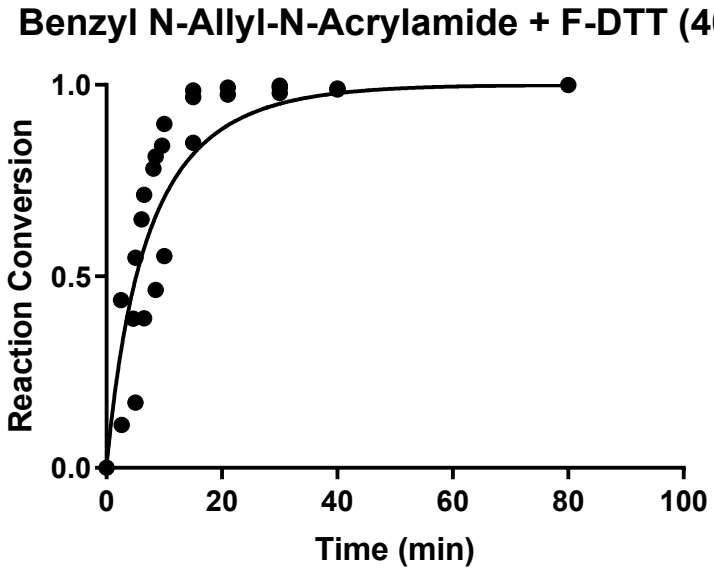

Figure S20. Observed 40°C kinetics by DTDP assay of 30 mM hydroxylated fluorous thiol (F-DTT) with 2 eqv of benzyl N-allyl-N-acrylamide catalyzed as described in the Methods (*n=3*).

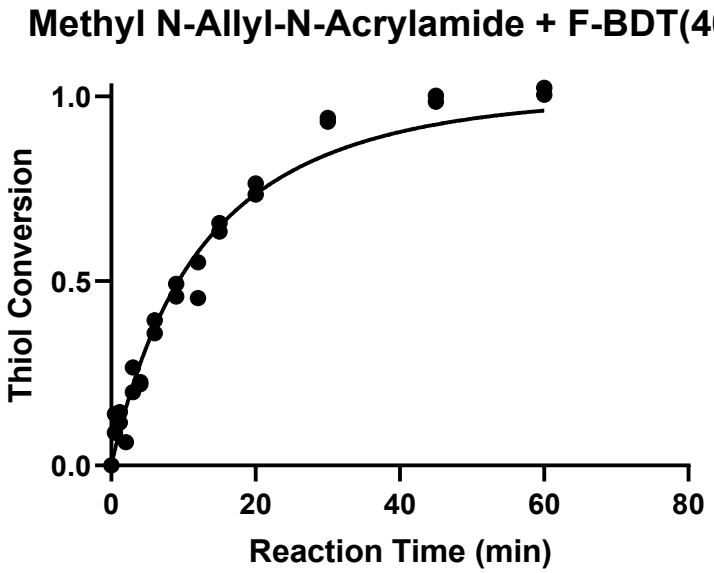

Figure S21. Observed 40°C kinetics by DTDP assay of 30 mM alkyl fluorous thiol (F-BDT) with 2 eqv of methyl N-allyl-N-acrylamide catalyzed as described in the Methods (*n=2*).

Effect of Explicit Methanol Solvent Molecules on Energy Barriers

To improve upon the use of an implicit CPCM methanol solvation model alone, we included four explicit methanol molecules at the thiolate hydroxyl groups to capture the effect of methanol on the hydrogen bonding energy. Figure S23 shows the comparison in barrier height for the case of only implicit solvent and implicit + explicit solvent for the butyl *N*-allyl-*N*-acrylamide mechanism.

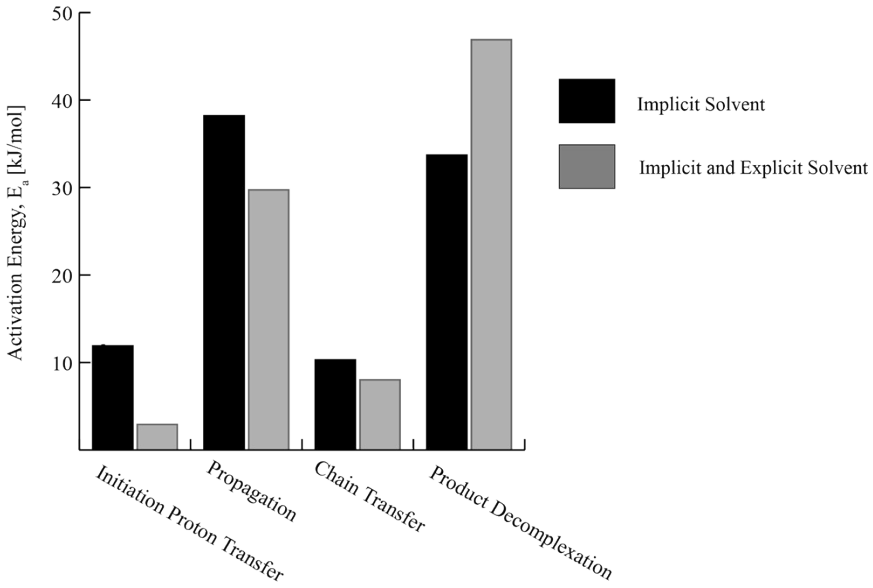

Figure S22. Energy barrier height for the butyl *N*-allyl-*N*-acrylamide mechanism with the CPCM implicit methanol solvent alone (black) and the inclusion of four explicit methanol solvents as well (grey).

For a full comparison of the energy barriers calculated by implicit solvent and explicit + implicit solvent, refers to the tables below. All data provided is in kJ/mol.

Table S6. The calculated energy barrier heights, calculated in DFT with the implicit CPCM methanol solvent and four explicit methanol molecules. Experimental values and error are reported as well. Bolded values show the rate limiting step. All units are kJ/mol.

	Initiation	Propagation	Chain Transfer	Product Decomplexation	Experiment	Error
Methyl (Alkyl)	0.0	24.6	1.6	**29.2**	17.8	11.4
Methyl	1.8	31.8	15.3	**40.7**	39.8	0.9
Butyl	3.9	29.7	8.0	**47.3**	51.6	-4.3
Hexyl	3.9	33.3	8.5	**47.1**	47.2	-0.1
Benzyl	7.7	31.3	8.8	**59.6**	108.4	-48.8
Ethylene Phenyl	0.8	35.2	6.6	**46.4**	28.1	18.3

Table S7. The calculated energy barrier heights, calculated in DFT with the implicit CPCM methanol solvent. Experimental values and error are reported as well. Bolded values show the rate limiting step. All units are kJ/mol.

	Initiation	Propagation	Chain Transfer	Product Decomplexation	Experiment	Error
Methyl (Alkyl)	3.8	**17.9**	4.2	17.7	17.8	0.1
Methyl	5.4	36.3	13.7	**37.0**	39.8	-2.8
Butyl	11.9	**40.6**	10.3	33.7	51.6	-11.0
Hexyl	9.0	**44.6**	10.8	34.2	47.2	-2.6
Benzyl	8.0	50.3	9.4	**54.0**	108.4	-54.4
Ethylene Phenyl	5.5	38.5	9.1	**46.0**	28.1	17.9

Geometry of Stationary Points

The Cartesian coordinates, along with the calculated energies for each stationary point can be found in the supplementary files "coordinates.xyz."

Supporting NMR and LCMS Spectra

All compounds within this study have been synthesized and reported before in prior publications by M Porel and C A Alabi., Journal of American Chemical Society. 136. (2014) pp 13162-13165 as well as J S Brown et al., Macromolecules. 50 (2017) pp 8731-8738. However, spectra of the compounds in this study are included.

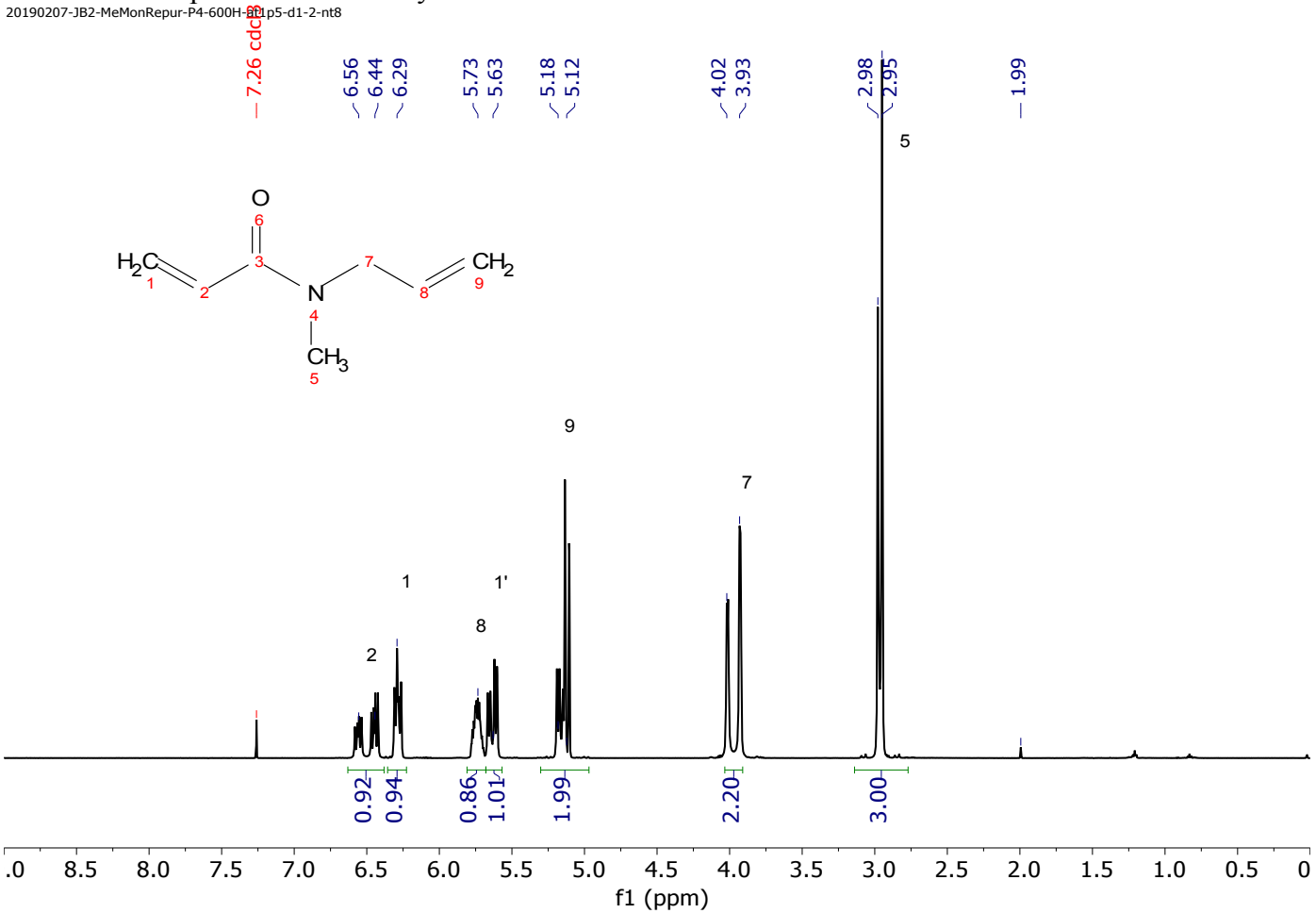

Methyl *N*-allyl-*N*-acrylamide. ^{1}H NMR (600 MHz, Chloroform-d) δ 6.51 (m, 1H), 6.29 (m, 1H), 5.73 (m, 1H), 5.63 (m, 1H), 5.15 (m, 2H), 3.98 (m, 2H), 2.97 (d, J = 17.6 Hz, 3H).

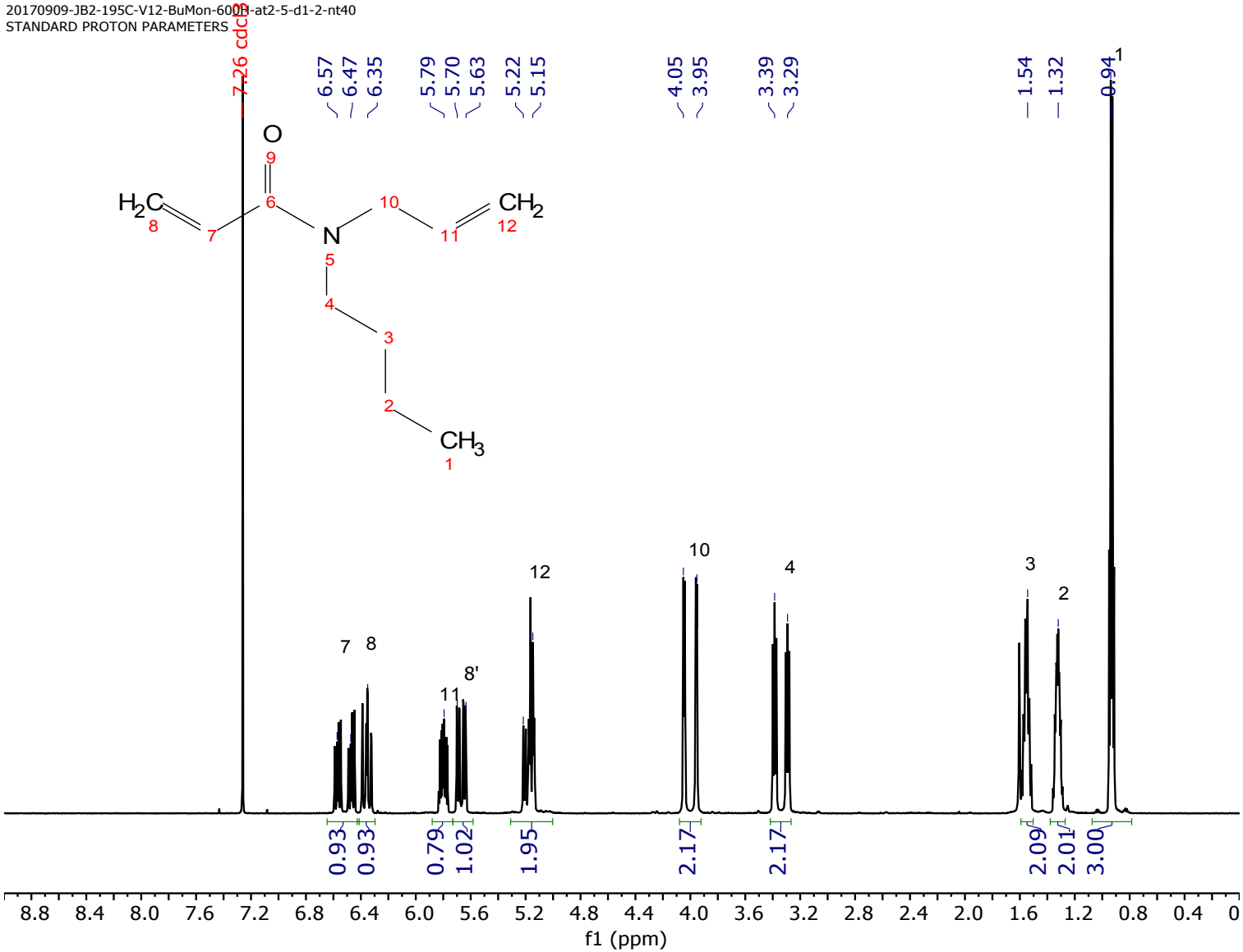

Butyl *N*-allyl-*N*-acrylamide. ^{1}H NMR (600 MHz, Chloroform-*d*) δ 6.52 (d, 1H), 6.35 (m, 1H), 5.79 (m, 1H), 5.67 (ddd, J_1 = 28.1 Hz, J_2 = 10.6 Hz, J_3 = 2.0 Hz, 1H), 5.18 (m, 2H), 4.00 (m, 2H), 3.34 (m, 2H), 1.54 (m, 2H), 1.32 (m, 2H), 0.94 (dd, $J_{1,2}$ = 7.21).

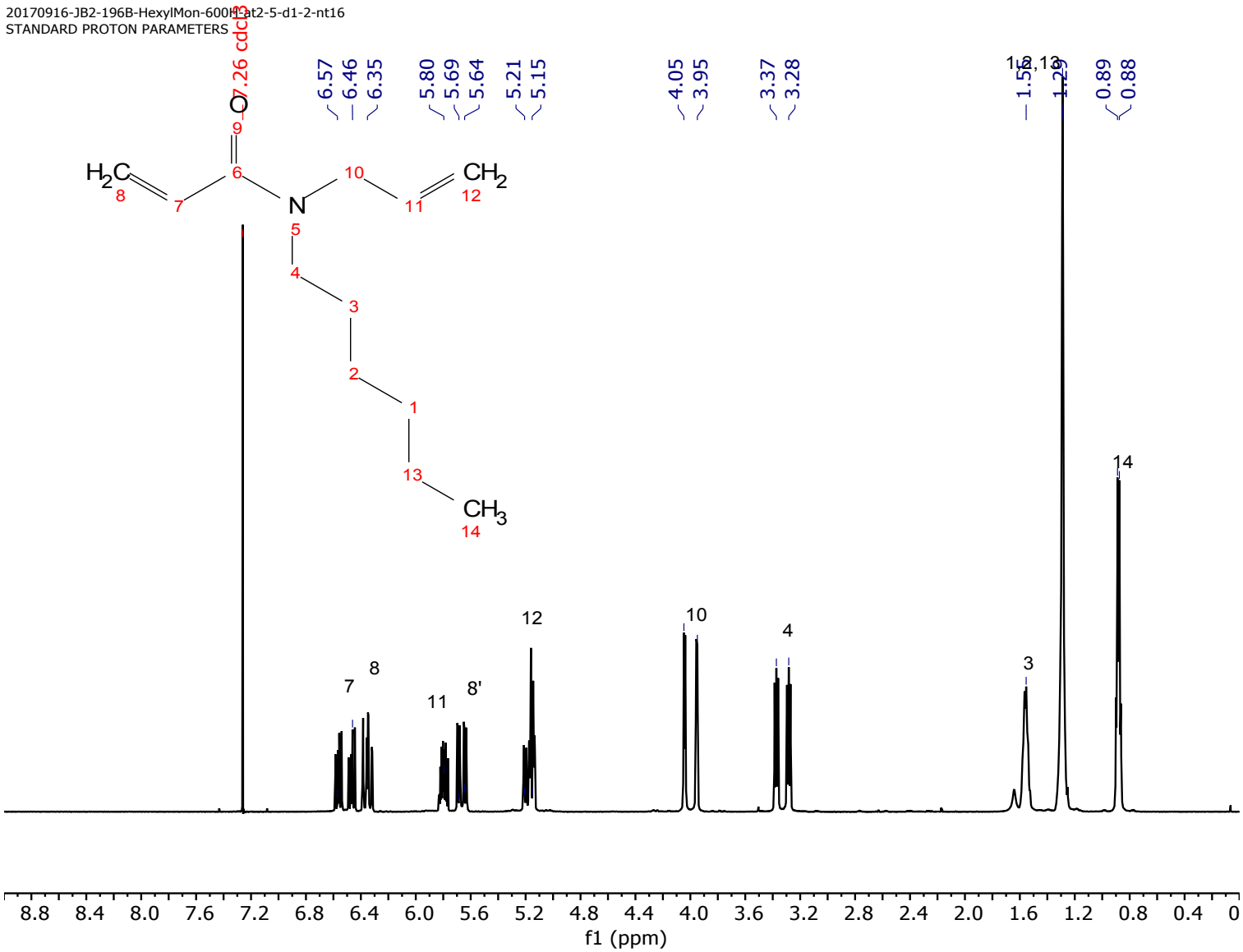

Hexyl *N*-allyl-*N*-acrylamide. ^{1}H NMR (600 MHz, Chloroform-*d*) δ 6.52 (m, 1H), 6.35 (m, 1H), 5.80 (m, 1H), 5.67 (ddd, J_1 = 28.7 Hz, J_2 = 10.4 Hz, J_3 = 2.0 Hz, 1H), 5.18 (m, 2H), 4.00 (m, 2H), 3.33 (m, 2H), 1.55 (m, 2H), 1.29 (m, 6H), 0.88 (m, 3H).

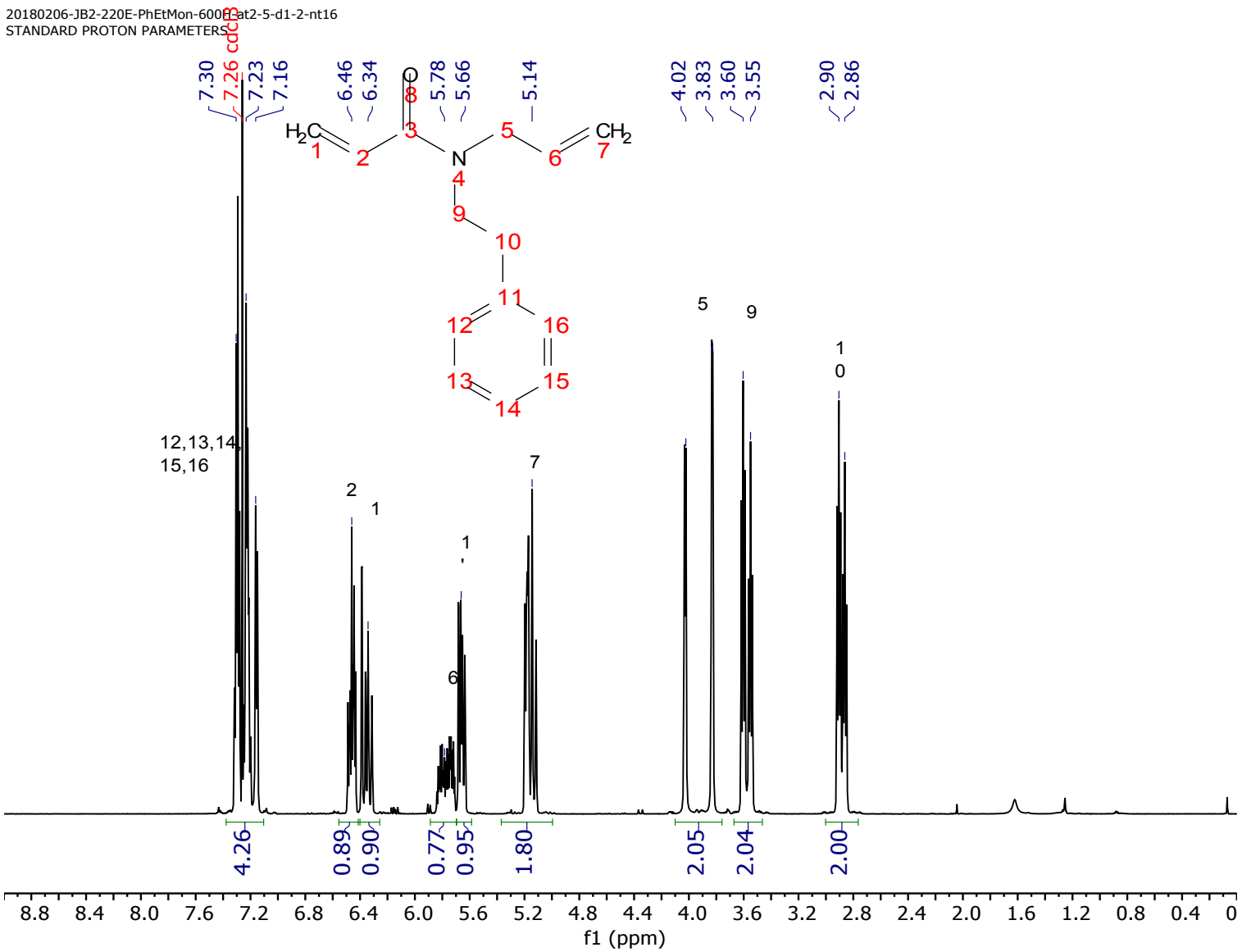

Ethylene Phenyl *N*-allyl-*N*-acrylamide. ^{1}H NMR (600 MHz, Chloroform-*d*) δ 7.38 – 7.10 (m, 5H), 6.46 (m, 1H), 6.34 (m, 1H), 5.78 (m, 1H), 5.66 (m, 1H), 5.14 (m, 2H), 3.92 (m, 2H), 3.58 (m, 2H), 2.88 (m, 2H).

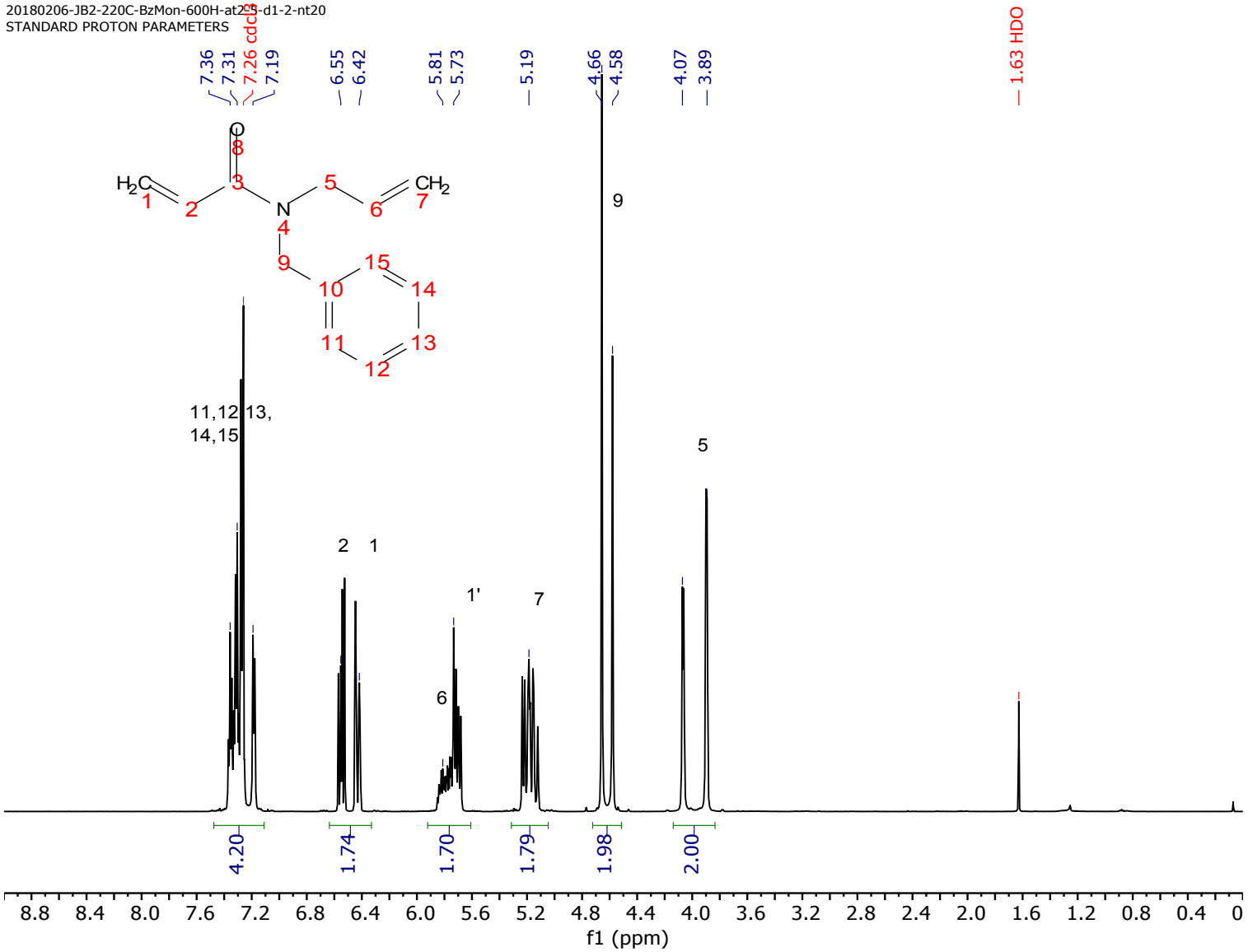

Benzyl *N*-allyl-*N*-acrylamide. ^{1}H NMR (600 MHz, Chloroform-*d*) δ 7.48 – 7.11 (m, 5H), 6.49 (m, 2H), 5.77 (m, 2H), 5.19 (s, 2H), 4.62 (d, J = 46.5 Hz, 2H), 3.98 (m, 2H).

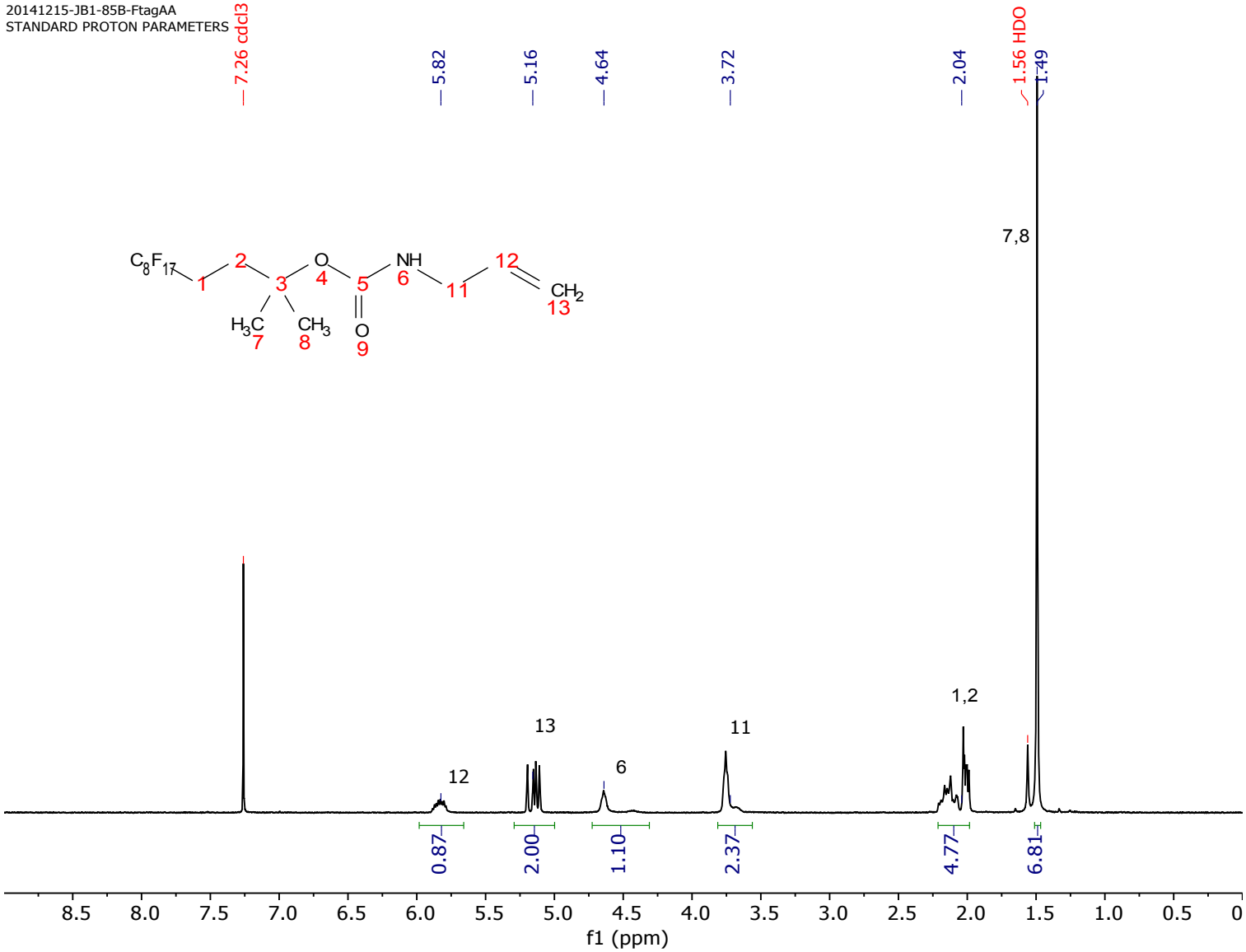

^{1}H NMR of "fluorous allyl amine" or 5,6,6,7,7,8,8,9,9,9-decafluoro-2-methyl-5-(perfluorobutyl)nonan-2-yl allylcarbamate in d-chloroform. ^{1}H NMR (400 MHz, Chloroform-*d*) δ 5.82 (m, 1H), 5.16 (m, 2H), 4.64 (m, 1H), 3.72 (s, 2H), 2.04 (m, 4H), 1.49 (s, 6H).

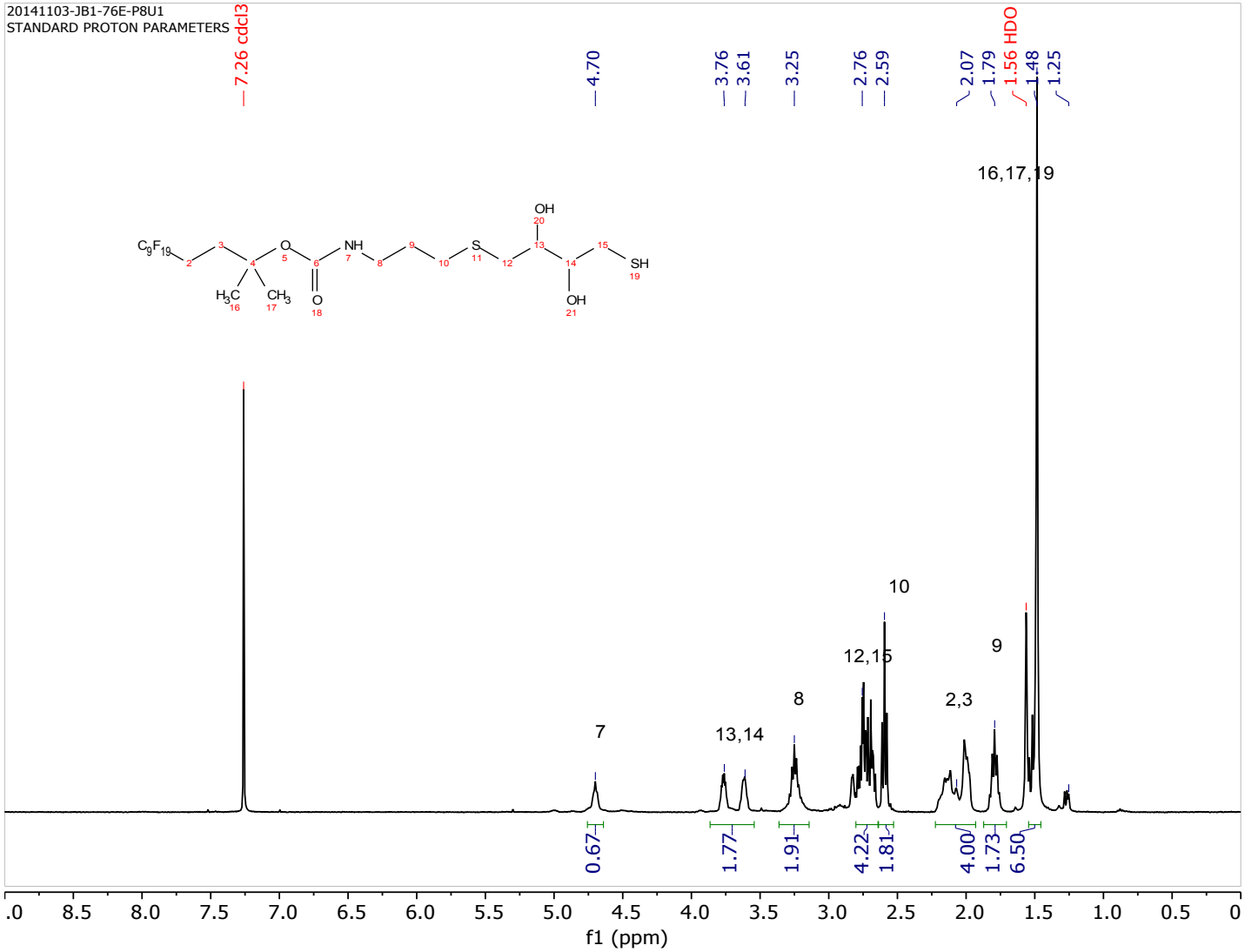

[1]H NMR of "fluorous DTT" the fluorous purified product of the thiolene reaction of fluorous allyl amine and DTT in d-chloroform. Note the disappearance of the allyl peaks. [1]H NMR (400 MHz, Chloroform-d) δ 5.82 (m, 1H), 5.16 (m, 2H), 4.64 (m, 1H), 3.72 (m, 2H), 2.04 (m, 4H), 1.49 (s, 7H).

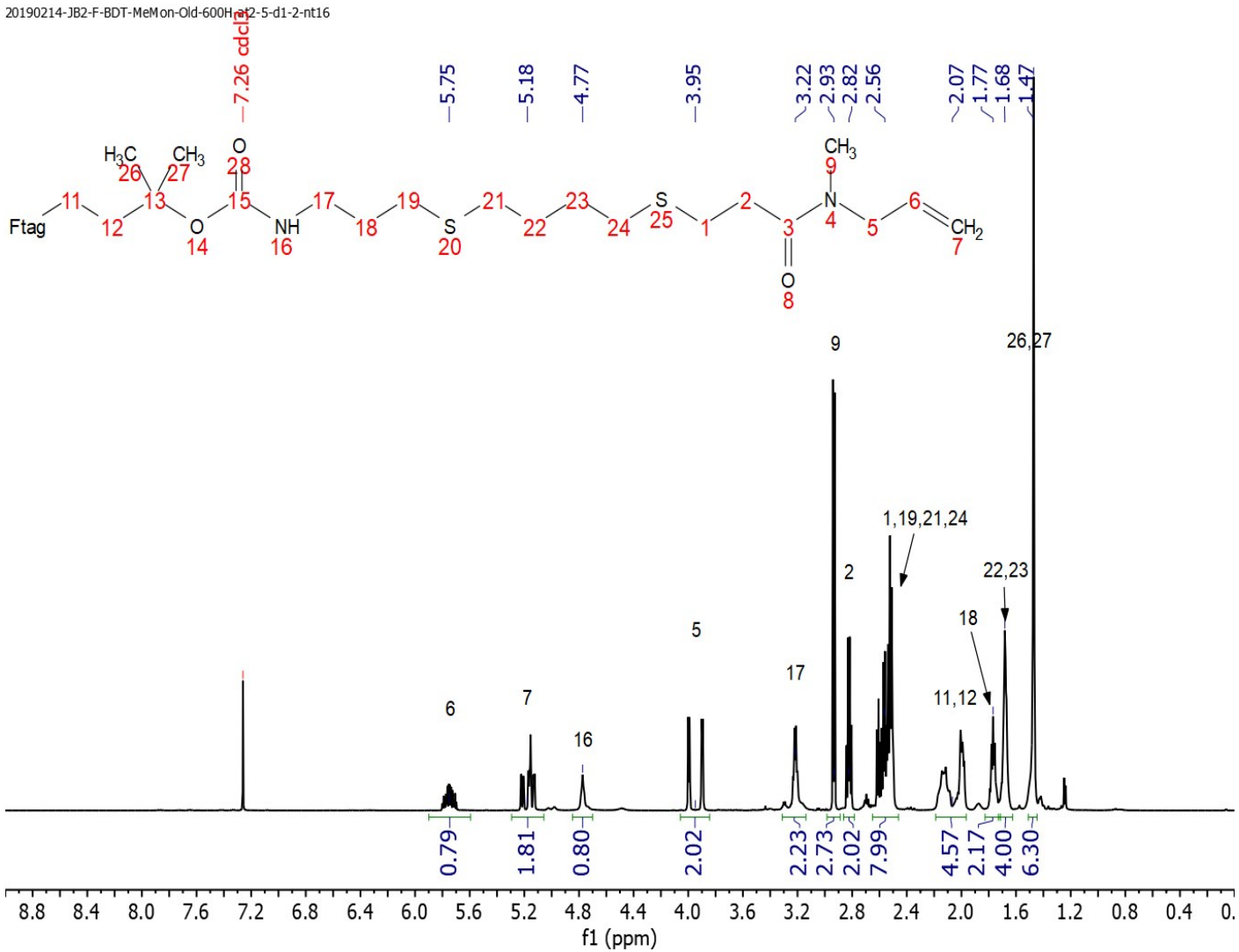

^{1}H NMR of "F-BDT-MeMon" in d-chloroform from the reaction of fluorous-BDT + MeMon. Representative NMR after fluorous solid-phase extraction after DTDP assay showed completion. ^{1}H NMR (600 MHz, Chloroform-*d*) δ 5.75 (m, 1H), 5.18 (m, 2H), 4.77 (m, 1H), 3.95 (m, 2H), 3.22 (m, 2H), 2.93 (d, J = 7.1 Hz, 3H), 2.82 (q, J = 7.4 Hz 2H), 2.56 (m, 8H), 2.07 (m, 4H), 1.77 (m, 2H), 1.68 (m, 4H), 1.47 (s, 6H).

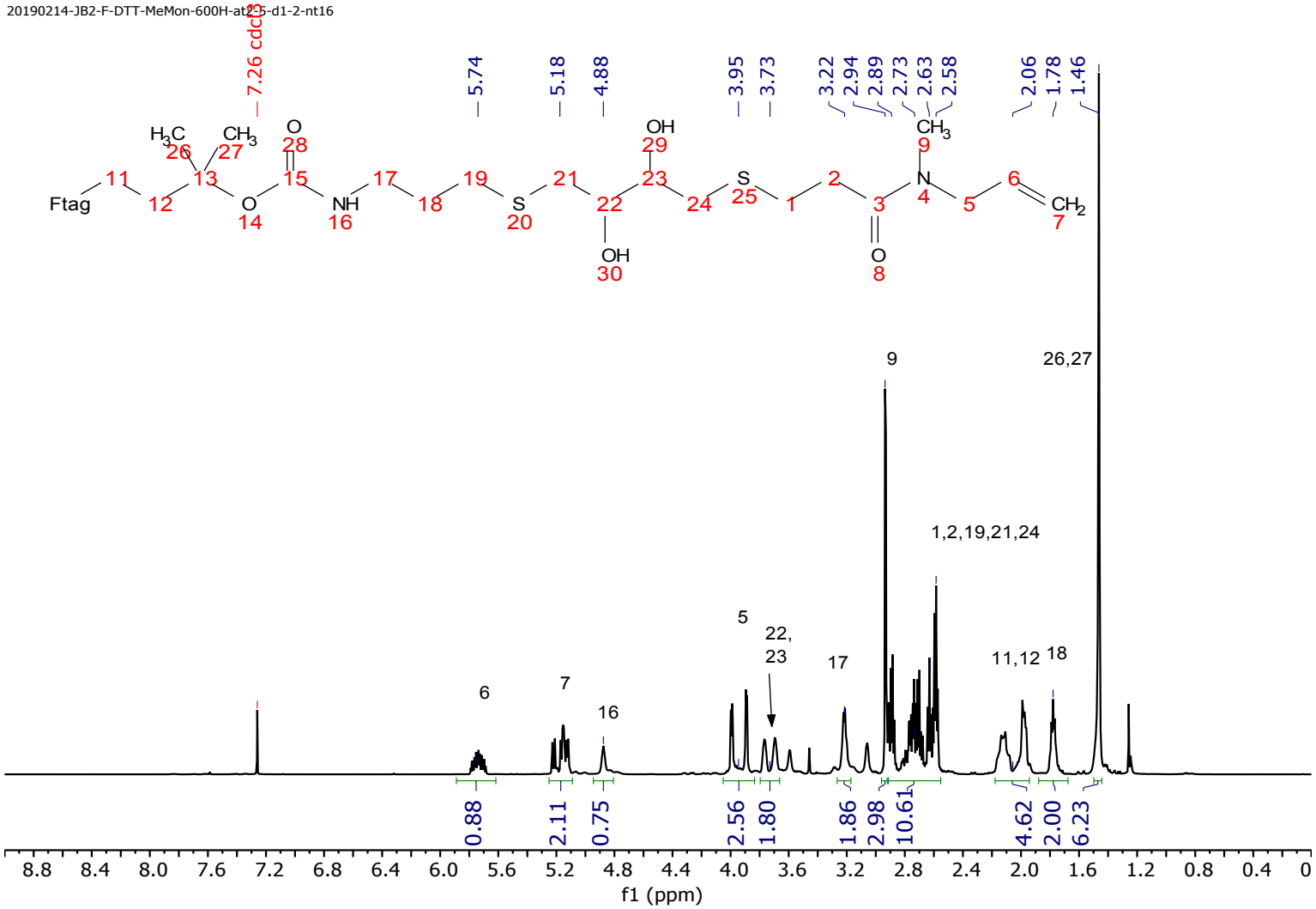

[1]H NMR of "F-DTT-MeMon" in d-chloroform from the reaction of fluorous-DTT + MeMon. Representative NMR after fluorous solid-phase extraction after DTDP assay showed completion. [1]H NMR (600 MHz, Chloroform-*d*) δ 5.74 (m, 1H), 5.18 (m, 2H), 4.88 (m, 1H), 3.95 (m, 2H), 3.73 (m, 2H), 3.22 (m, 2H), 2.94 (d, *J* = 3.6 Hz, 3H), 2.92 – 2.56 (m, 11H), 2.06 (m, 4H), 1.78 (m, 2H), 1.46 (s, 6H).

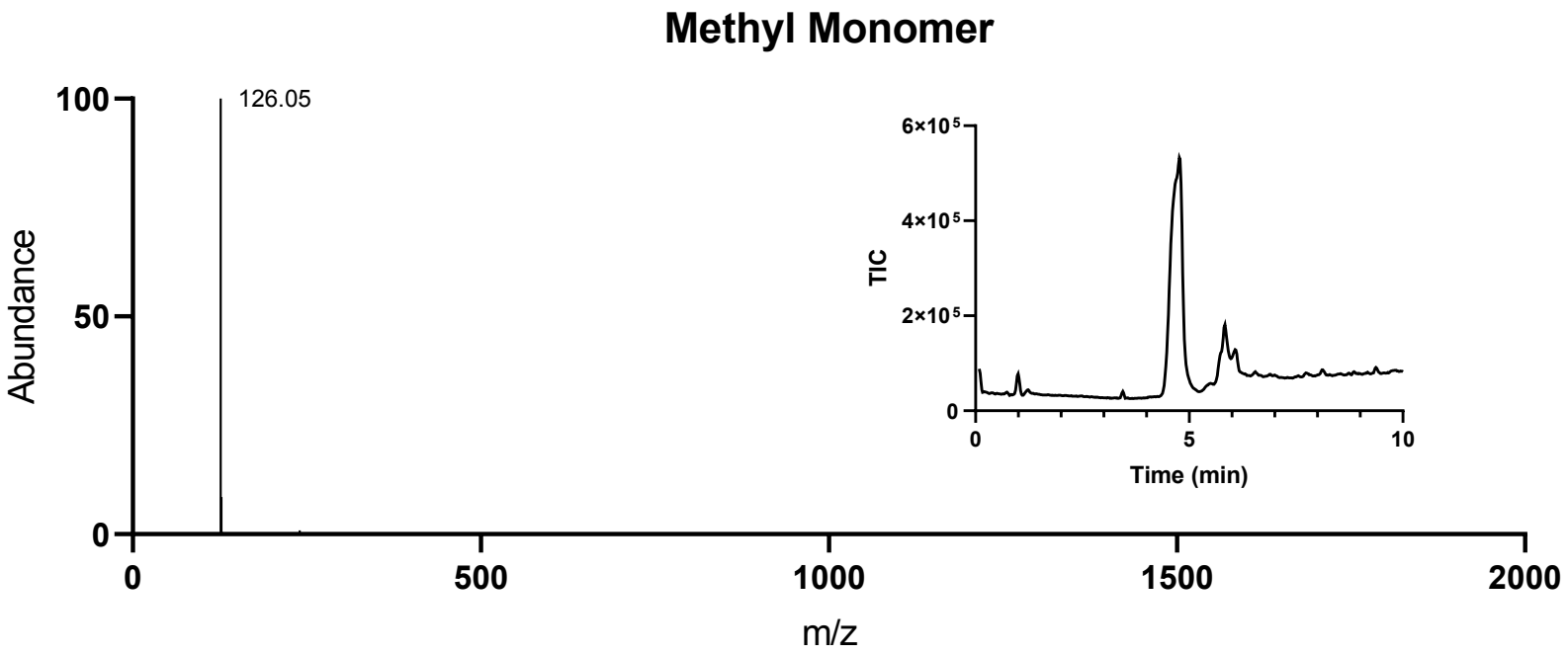

High performance liquid chromatography mass spectrometry (LCMS) of methyl *N*-allyl-*N*-acrylamide operating in positive ion mode. The inset graph contains the total ion count (TIC) over the 10-minute (5-100%) gradient. Mass spectra displayed is from 4.31-5.14 minutes Expected mass 126.09; observed 126.05.

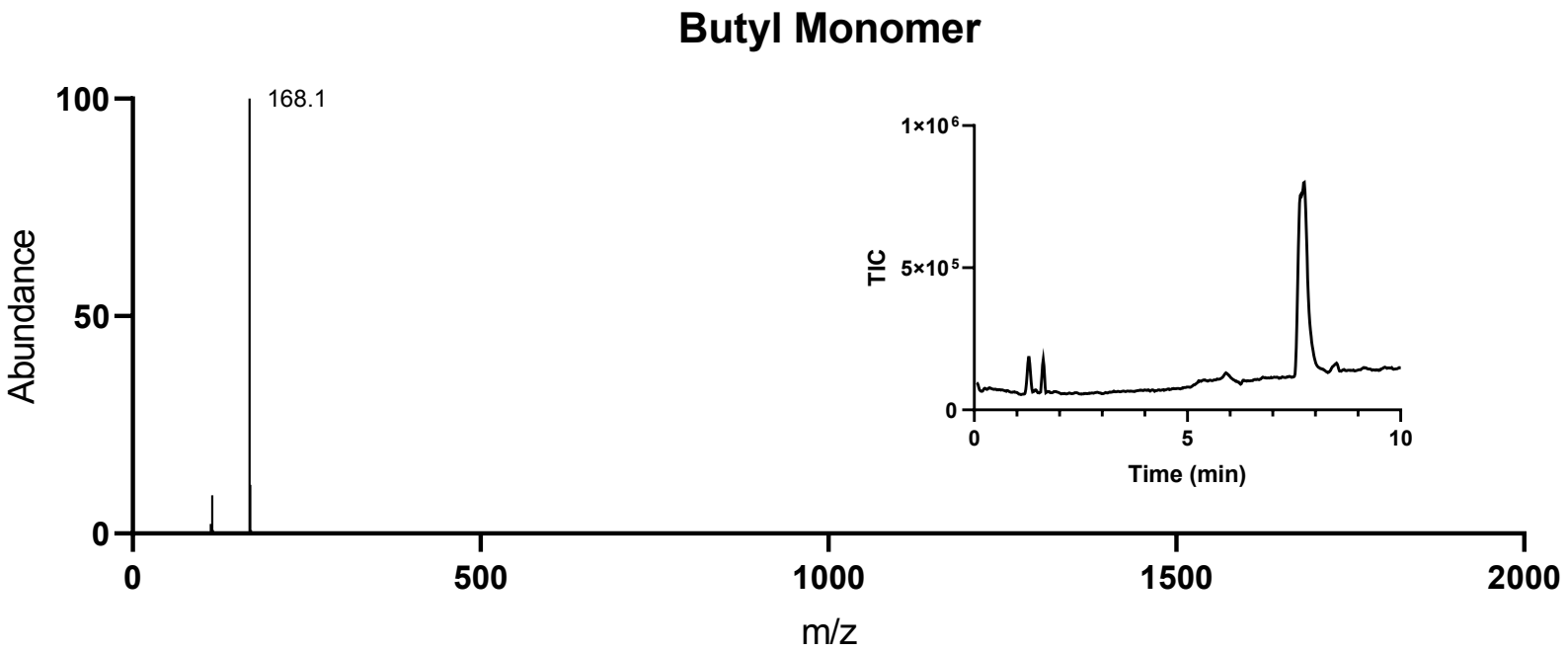

High performance liquid chromatography mass spectrometry (LCMS) of butyl *N*-allyl-*N*-acrylamide operating in positive ion mode. The inset graph contains the total ion count (TIC) over the 10-minute (5-100%) gradient. Mass spectra displayed is from 7.47-8.14 minutes Expected mass 168.14; observed 168.1.

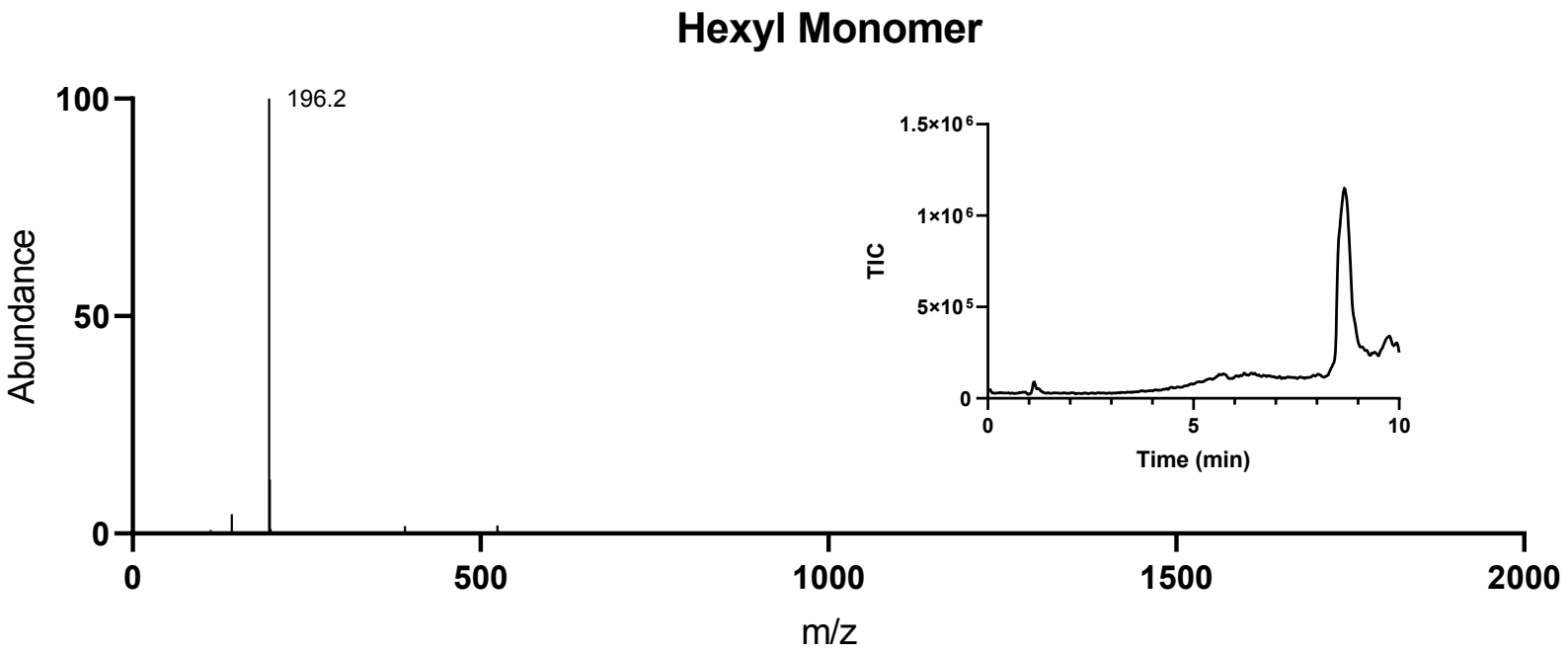

High performance liquid chromatography mass spectrometry (LCMS) of hexyl *N*-allyl-*N*-acrylamide operating in positive ion mode. The inset graph contains the total ion count (TIC) over the 10-minute (5-100%) gradient. Mass spectra displayed is from 8.36-9.19 minutes Expected mass 196.17; observed 196.2.

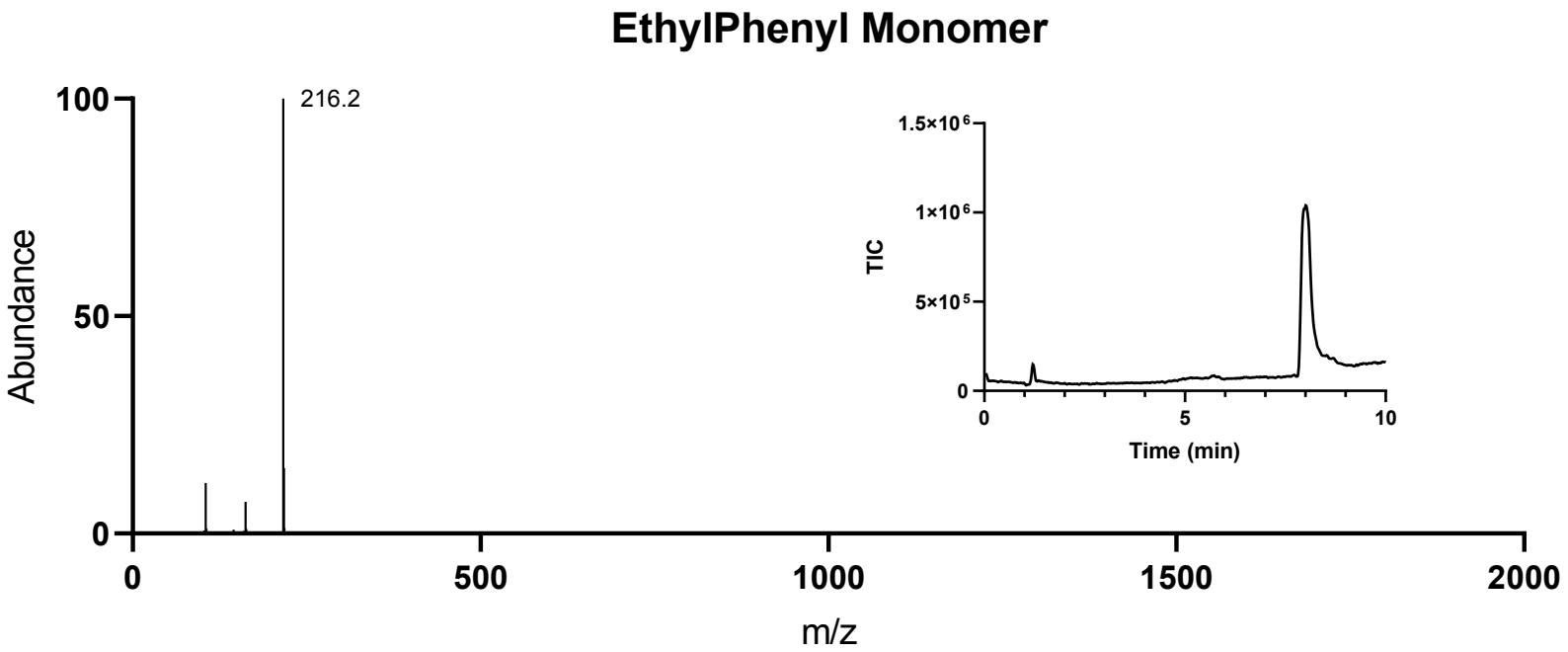

High performance liquid chromatography mass spectrometry (LCMS) of ethylenephenyl *N*-allyl-*N*-acrylamide operating in positive ion mode. The inset graph contains the total ion count (TIC) over the 10-minute (5-100%) gradient. Mass spectra displayed is from 7.77-8.69 minutes Expected mass 216.14; observed 216.2.

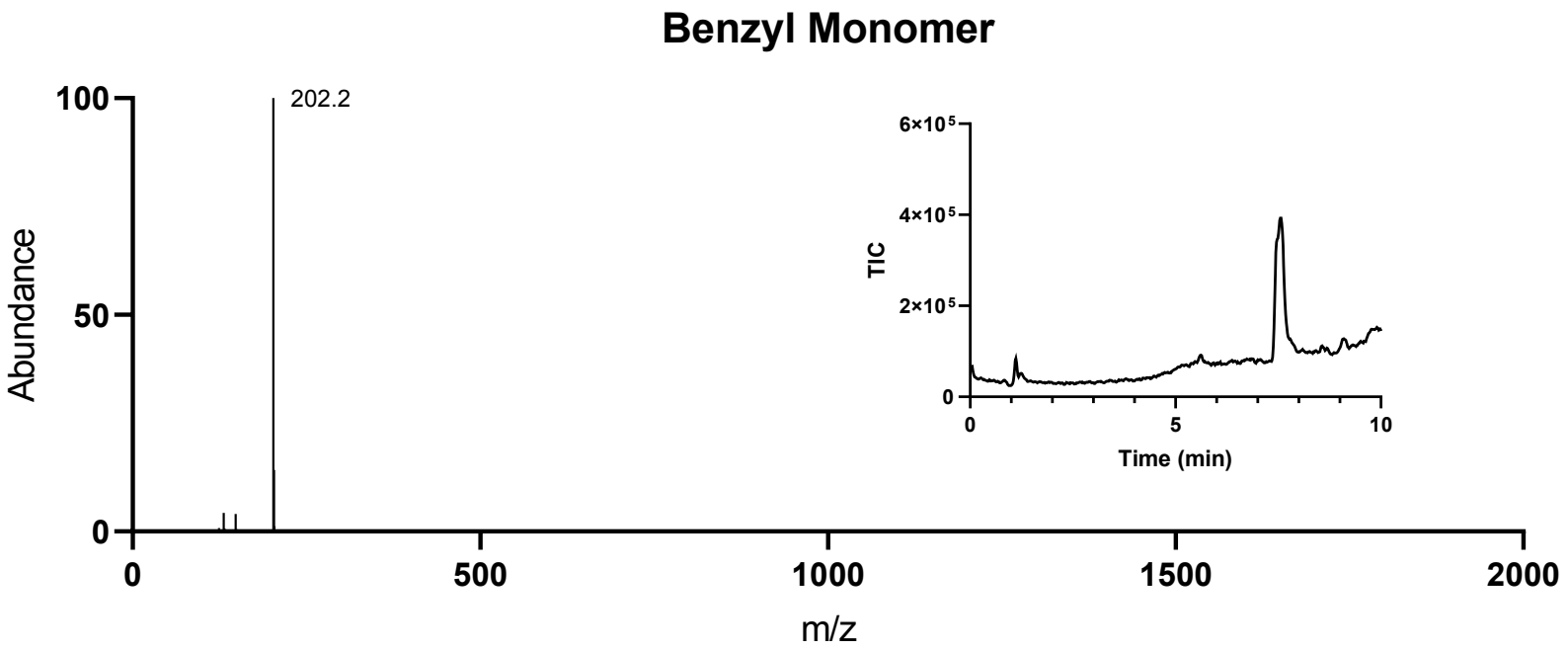

High performance liquid chromatography mass spectrometry (LCMS) of benzyl *N*-allyl-*N*-acrylamide operating in positive ion mode. The inset graph contains the total ion count (TIC) over the 10-minute (5-100%) gradient. Mass spectra displayed is from 7.33-7.94 minutes Expected mass 202.12; observed 202.2.

References

1. Egwim, I. O. & Gruber, H. J. Spectrophotometric measurement of mercaptans with 4,4'-dithiodipyridine. *Anal. Biochem.* **288**, 188–194 (2001).
2. Grassetti, D. R. & Murray, J. F. Determination of sulfhydryl groups with 2,2'- or 4,4'-dithiodipyridine. *Arch. Biochem. Biophys.* **119**, 41–49 (1967).
3. Smith, J. M., Jami Alahmadi, Y. & Rowley, C. N. Range-separated DFT functionals are necessary to model thio-Michael additions. *J. Chem. Theory Comput.* **9**, 4860–4865 (2013).
4. Goerigk, L. *et al.* A look at the density functional theory zoo with the advanced GMTKN55 database for general main group thermochemistry, kinetics and noncovalent interactions. *Phys. Chem. Chem. Phys.* **19**, 32184–32215 (2017).
5. Mardirossian, N. & Head-Gordon, M. Thirty years of density functional theory in computational chemistry: An overview and extensive assessment of 200 density functionals. *Mol. Phys.* **115**, 2315–2372 (2017).
6. Awoonor-Williams, E. *et al.* Quantum Chemical Methods for Modeling Covalent Modification of Biological Thiols. *J. Comput. Chem.* **41**, 427–438 (2020).
7. Neese, F. The ORCA program system. *Wiley Interdiscip. Rev. Comput. Mol. Sci.* **2**, 73–78 (2012).
8. Grimme, S. Semiempirical GGA-type density functional constructed with a long-range dispersion correction. *J. Comput. Chem.* **27**, 1787–1799 (2006).
9. Schäfer, A., Horn, H. & Ahlrichs, R. Fully optimized contracted Gaussian basis sets for atoms Li to Kr. *J. Chem. Phys.* **97**, 2571–2577 (1992).
10. Weigend, F. & Ahlrichs, R. Balanced basis sets of split valence, triple zeta valence and quadruple zeta valence quality for H to Rn: Design and assessment of accuracy. *Phys. Chem. Chem. Phys.* **7**, 3297 (2005).
11. Weigend, F., Häser, M., Patzelt, H. & Ahlrichs, R. RI-MP2: optimized auxiliary basis sets and demonstration of efficiency. *Chem. Phys. Lett.* **294**, 143–152 (1998).
12. Cossi, M., Rega, N., Scalmani, G. & Barone, V. Energies, structures, and electronic properties of molecules in solution with the C-PCM solvation model. *J. Comput. Chem.* **24**, 669–681 (2003).
13. Nocedal, J. Updating quasi-Newton matrices with limited storage. *Math. Comput.* **35**, 773–773 (1980).
14. Herbol, H. C., Stevenson, J. & Clancy, P. Computational Implementation of Nudged Elastic Band, Rigid Rotation, and Corresponding Force Optimization. *J. Chem. Theory Comput.* **13**, 3250–3259 (2017).
15. Henkelman, G., Uberuaga, B. P. & Jónsson, H. A climbing image nudged elastic band method for finding saddle points and minimum energy paths. *J. Chem. Phys.* **113**, 9901–9904 (2000).
16. Frayne, S. H. & Northrop, B. H. Evaluating Nucleophile Byproduct Formation during Phosphine- and Amine-Promoted Thiol-Methyl Acrylate Reactions. *J. Org. Chem.* **83**, 10370–10382 (2018).
17. Rai, N. & Siepmann, J. I. Transferable potentials for phase equilibria. 9. Explicit hydrogen description of benzene and five-membered and six-membered heterocyclic aromatic compounds. *J. Phys. Chem. B* **111**, 10790–10799 (2007).